Construction of NMR equipment to be used in the Physical Properties Measurement System (PPMS, Quantum Design)

Alexander Gafner

Juli 2006

Acknowledgments

First I would like to thank Prof. Dr. Andreas Schilling for the opportunity of absolving this Diploma thesis in his group.

Special thanks go to Dr. Joseph Roos for his advisory guiding, support, and for the numerous discussions through this work.

A special thank goes to the members of the institutes workshop for the help on the construction of the NMR probe head and to Peter Soland for the advisory help on the building of the 70 MHz spectrometer.

To the Ph.D. student Simon Strässle, friend and office-mate, I'm thankful for the inspiring discussions.

Y sobre todo le agradezco a mi queridisima familia por su apoyo, su paciencia y darme la oportunidad de estudiar esta carrera. También a mis amigos(as) y coinquilinos(as) con que he convivido en todo este tiempo les agradezco.

Contents

Chapter 1

Introduction

In the first half of the 20th century, with the increasing knowledge and understanding of quantum mechanics, resonance experiments became more and more important. Experimental techniques using electrons and the nuclei where developed. *Nuclear magnetic resonance* NMR makes use of the interaction of the nuclei with its electric and magnetic surroundings (chapter 2). Using the nuclei as a local probe being positioned directly in the sample opens various possibilities to study materials and compounds in different areas of natural science and medicine. In material and solid-state physics research the solid-state NMR is widely applied to crystals and powder samples.

The goal of this diploma thesis is to implement an NMR system to be used with the *Physical Properties Measurement System* (PPMS) manufactured by Quantum Design, with the possibility of driving the magnetic field up to $9\,\mathrm{T}$ and the temperature down to $1.8\,\mathrm{K}$. Such a system then opens the opportunity of performing field scans and extending the cooling range for NMR experiments at this institute. The NMR apparatus (chapter 3) was extended by the construction of a new NMR probe head and a new spectrometer (chapter 4), which were tested on functionality and performance (chapter 5).

Finally the constructed elements where applied to do investigation on the ^{139}La, ^{137}Ba, and ^{135}Ba nuclei of $LaBaNiO_{4-\delta}$ (chapter 6), which is thought to be a candidate to represent a "parent compound" of Ni-based superconductors. The main goal of our NMR study is to investigate the temperature and field behavior of the quadrupole effects (chapter 2) and to clarify if there is any magnetic Ni-spin ordering.

1

Chapter 2

Theory

Nuclear magnetic resonance (NMR) makes use of the interaction of atomic nuclei with its surroundings, which are of electrical and magnetic nature, using the nucleus as a highly sensitive sensor at an atomic level. Already small samples (10^{21} to 10^{23} spins), liquid or solid, can give conclusive experimental results about its magnetic properties, microscopic buildup, and phase transitions. The continuing NMR evolution began in the 1940's and has today meaningful applications in many scientific subjects, for instance in chemistry, biology, geology, medicine, archaeology, and physics.

In this NMR theory section we will restrain to introduce the NMR basics and present shortly the used methods and expected effects. For deeper consideration we cite the NMR text books of A. Abragam Ref. [1] and C. P. Slichter Ref. [2].

2.1   NMR basics

For a nucleus we have a relation between the total angular momentum $\vec{J}$ and the magnetic dipole moment

$$\vec{\mu} = \gamma \vec{J} \ . \tag{2.1}$$

γ is the gyromagnetic ratio, a scalar nucleus dependent number. $\vec{J}$ can be written as $\vec{J} = \hbar \vec{I}$, with $\vec{I}$ being the nuclear spin operator. An applied static magnetic field $\vec{B}_0$ interacts with the magnetic moment of the nucleus described by the Hamiltonian operator

$$\mathcal{H} = -\vec{\mu} \cdot \vec{B}_0 \ . \tag{2.2}$$

Assuming $\vec{B}_0$ is aligned parallel to the z-axis we get

$$\mathcal{H} = -\mu_z B_0 = -\gamma \hbar B_0 I_z \ . \tag{2.3}$$

I_z describes the projection of $\vec{I}$ to the quantization axis. $\vec{B}_0$ causes a splitting of the degenerated states into $2I + 1$ equidistant energy eigenvalues of the form:

$$E_m = -\gamma \hbar B_0 m \quad \text{with} \quad m = I, I - 1, \ldots, -I \ . \tag{2.4}$$

This energy splitting induced by an external static magnetic field, is called the "nuclear Zeeman effect".

Building the energy eigenvalue $E_m = \langle m|\mathcal{H}|m\rangle$, we get the energy relation

$$\hbar\omega = \Delta E = E_m - E_{m+1} = \gamma\hbar B_0 \ . \tag{2.5}$$

ΔE is the energy difference between the split energy levels ($|\Delta m| = 1$). With this we obtain the angular Larmor frequency

$$\omega_L = \gamma B_0 \ . \tag{2.6}$$

From thermodynamics we know that the occupation of the energy levels in thermal equilibrium follows the Boltzmann distribution

$$P(E_m) \propto \exp(-E_m/k_B T) \ . \tag{2.7}$$

This unequal population of the energy levels produces a polarization of the nuclear spin system. By summing all the magnetic moments per volume unit and writing out the nuclear spin polarization $\langle I_z\rangle$, we get the magnetization $\vec{M}$

$$\vec{M}_z \ = \ \sum_i \frac{\vec{\mu}_{iz}}{V} = N\gamma\hbar\langle I_z\rangle \tag{2.8}$$

$$\text{with} \quad \langle I_z\rangle \ = \ \frac{\gamma\hbar I(I+1)B}{3k_B T} \tag{2.9}$$

$$\implies \quad \vec{M} \ = \ N\frac{\gamma^2\hbar^2 I(I+1)}{3k_B T}\vec{B} \ , \tag{2.10}$$

where N is the nuclear spin density.

The split energy multiplets can be detected when transitions between these levels occur induced by alternating electromagnetic fields. If we apply an oscillating magnetic field $\vec{B}_1$ along the x-axis, which is perpendicular to $\vec{B}_0$, equation (2.3) reads

$$\mathcal{H} = -\gamma\hbar B_0 I_z - \gamma\hbar B_1 I_x \cos\omega t \ . \tag{2.11}$$

The motion of the magnetic dipole moment under the influence of the static field $\vec{B}_0$ and the oscillating field $\vec{B}_1$ can be described in a system rotating with angular frequency ω (see Ref. [2]) by

$$\frac{d\vec{\mu}}{dt} = \vec{\mu} \times \gamma\vec{B}_{eff} \qquad \text{with} \qquad \vec{B}_{eff} = (B_0 - \frac{\omega}{\gamma})\vec{e}_z + B_1\vec{e}_x \ . \tag{2.12}$$

This means that, observed in the rotating system, the magnetic moment feels an effective static magnetic field $\vec{B}_{eff}$. The moment $\vec{\mu}$ precesses along a cone surface with a constant

angle around the axis of $\vec{B}_{eff}$ having an angular frequency of γB_{eff}.

In resonance, i.e. with $\omega = \gamma B_0$, the effective field is equal to $B_1 \vec{e}_x$. A moment being aligned along the z-axis will rotate in the yz-plane of the rotating system. If $\vec{B}_1$ is applied for the time span t_p the moment turns by an angle $\alpha = \gamma B_1 t_p$. By choosing B_1 and t_p so, that $\alpha = \pi$, the magnetic moment inverts its orientation. The corresponding pulse is called a 180°-pulse. If we set the field and the time span to get $\alpha = \pi/2$ a 90°-pulse is generated and the magnetic moment will have rotated from the z-direction to the y-direction observed in the rotating system. As soon as the 90°-pulse is over, the magnetic moment will precess in the laboratory system around the direction of the static magnetic field $\vec{B}_0$ along the z-axis.

Applying a pulse on a sample results in an energy and temperature gain of the spin system. Due to relaxation processes energy is transfered between the spin system and its surroundings. Since the spin system is coupled to the lattice, the latter is capable to absorb this energy, which is described in more detail in Ref. [2].

The possible relaxation channels are of magnetic and electrical type. The perturbed spin system returns to thermal equilibrium due to fluctuating local magnetic fields which is the so called magnetic relaxation. In simple metals the relaxation is dominated by the magnetic Fermi-contact interaction of the nuclear spins with the spins of the conduction electrons.

If the relaxation is produced by fluctuations of the *electric field gradient* EFG at the nuclear sites, it is a quadrupolar relaxation (see section 2.4).

2.2 Bloch equations

For two energy levels, only one transition is possible. Let us define N_+^0 and N_-^0 as the population numbers in thermal equilibrium, then $n = N_+^0 - N_-^0$ denotes the population difference between the levels. Assuming Maxwell-Boltzmann-statistics we can write the population ratio as follows:

$$\frac{N_-^0}{N_+^0} = \exp\left(-\frac{\Delta E}{k_B T}\right) . \tag{2.13}$$

If there is a mechanism which induces transitions between the two energy levels, a rate can be defined as

$$\frac{dN_+}{dt} = N_- W_\downarrow - N_+ W_\uparrow . \tag{2.14}$$

$W_\uparrow$ and $W_\downarrow$ denote the probability of inducing a spin transition upward and downward in energy, respectively. By defining the total population number as $N = N_+ + N_-$, the

difference of the population number $n = N_+ - N_-$ can be written as

$$\frac{dn}{dt} = N(W_\downarrow - W_\uparrow) - n\left(W_\downarrow + W_\uparrow\right) \ ,\tag{2.15}$$

which is equivalent to

$$\frac{dn}{dt} = \frac{n_0 - n}{T_1} \ ,\tag{2.16}$$

where

$$n_0 = N\left(\frac{W_\downarrow - W_\uparrow}{W_\downarrow + W_\uparrow}\right) \ ,\tag{2.17}$$

$$T_1 = \frac{1}{W_\downarrow + W_\uparrow} \ .\tag{2.18}$$

To solve (2.16) we take the basic exponential approach

$$n = n_0 + Ae^{-t/T_1} \ ,\tag{2.19}$$

where n_0 is the population difference in thermal equilibrium and T_1 the characteristic time, which the system needs to reach the thermal equilibrium. Analogous to equation (2.16), we get the phenomenological equation for the magnetization $M_z = \gamma\hbar n/2$ which is assumed to be parallel in the z-axis

$$\frac{dM_z}{dt} = \frac{M_0 - M_z}{T_1} \ ,\tag{2.20}$$

with M_0 the magnetization in thermal equilibrium. By combining (2.20) with the equation of motion of the magnetization $\vec{M}$ we get

$$\frac{dM_z}{dt} = \frac{M_0 - M_z}{T_1} + \gamma\left(\vec{M} \times \vec{B}\right)_z \ .\tag{2.21}$$

Since the magnetization in thermal equilibrium is aligned with the external static magnetic field $\vec{B}_0$, the components of the magnetization have to dissappear along the x-axis and the y-axis after the time T_2

$$\frac{dM_x}{dt} = \gamma\left(\vec{M} \times \vec{B}\right)_x - \frac{M_x}{T_2} \ ,\tag{2.22}$$

$$\frac{dM_y}{dt} = \gamma\left(\vec{M} \times \vec{B}\right)_y - \frac{M_y}{T_2} \ .\tag{2.23}$$

Combining equations (2.21), (2.23), and (2.22) we get the Bloch equation

$$\frac{d\vec{M}}{dt} = \gamma(\vec{M} \times \vec{B}) - \left(\frac{M_x\vec{e}_x + M_y\vec{e}_y}{T_2} - \frac{M_0 - M_z}{T_1}\vec{e}_z\right) \ .\tag{2.24}$$

The solution of the Bloch equation if a *radio frequency* (RF) field B_1 is applied, can be found in Refs. [1] and [2].

We resume the relaxation times.

T_1 : The *spin-lattice relaxation time* is a measure of the time for the energy exchange between the spin system and the lattice, being the time it takes for the magnetization to return to thermal equilibrium in the external magnetic field direction. Typical time values for solid-state materials are parts of ms until hours.

T_2 : The *spin-spin relaxation time* is the time the magnetic moments of the nuclear spins need to get out of phase in the plane perpendicu lar to the external magnetic field, causing a deacay of the magnetization in this plane. Typical values for T_2 are about $100\,\mu$s.

It is clear that T_2 cannot be larger than T_1.

2.3 Free induction decay and measuring methods

To resume, a spin system with no preferred direction shows a completely isotropic spin-orientation pattern. By applying an external magnetic field in the z-direction the spins order to be in an energetically favorable orientation. For the nuclear moments with a positive γ an antiparallel alignment is favorable. The presence of the external magnetic field splits the degenerated levels so that the Zeeman effect can be observed. The population of the m levels in thermal equilibrium follows the Boltzmann distribution shown in (2.7). This distribution describes the spin polarization (2.9) resulting in a magnetization $\vec{M}$ along the magnetic field (2.10). As there is no phase coherence of the spins, there is no transverse magnetization. Transitions are induced through a RF excitation pulse if an oscillating magnetic field $\vec{B}_1$ is applied perpendicular to $\vec{B}_0$ (via a coil) during the time t_p. The effect of this oscillation on the magnetic moment is described in (2.12).

This temporary disturbance rotates the magnetization with the Larmor frequency over a cone surface around the z-axis, observed from the laboratory system, producing a macroscopic magnetization component which rotates in the xy-plane. With an ideal 90°-pulse the full magnetization would completely rotate in the xy-plane. This xy-component rotating magnetization induces an electromotive force, i.e. a measurable response in an external detection coil. Through inhomogeneities of the external and/or internal local magnetic fields, the rotation frequencies of the spins are distributed, which makes the spins run out of phase. This fanning-out of the spins generates a loss of the transverse magnetization within the time T_2^{FID}. Finally the net transverse magnetization disappears. This decay is called the *free induction decay* (FID). An example of a FID shown in the left panel of figure 2.1.

This FID can be *Fourier transformed* (FT) from the time space into the frequency space, where peaks will appear at the responding frequencies visible in the right panel of figure 2.1. This is a very common NMR approach called *Fourier-transformed* NMR.
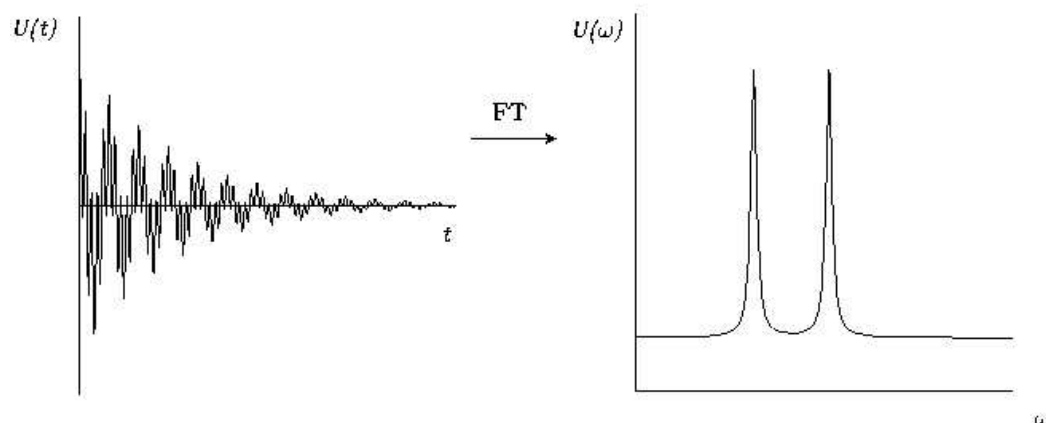
Figure 2.1: The FID shown in the left panel (frequency space) produces, after a Fourier transformation, a peak spectrum in the frequency space (right panel).

2.3.1   Pulse scheme

Through NMR history many different pulse schemes were developed. Generally used simple methods are the single-pulse FID analysis for spectral investigations, the *inversion-pulse* and *pulse-saturation method* for spin-lattice relaxation measurements, and the *spin-echo method* for spin-spin relaxation studies or spectral analysis. In this diploma thesis mainly the spin-echo method was used.

Spin-Echo method
The spin-echo method makes use of the refocusing of the spins. A 90°-pulse produces a rotating magnetization in the xy-plane which loses the coherence of its magnetic moments with time. After a spacing time τ a 180°-pulse is applied, producing an inversion of the spins. The spins refocus after another time τ, i.e. roughly 2τ after the 90°-pulse. In solid-state materials the FID usually decays very fast (parts of a ms), in some materials the decay of the signal is even so fast, that technical factors impede a proper detection. In this case the spin-echo method has to be applied. It is clear that τ has to be shorter than T_2 in order to assure a transverse magnetization component perpendicular to the external static field.

2.4 Frequency broadening

Besides the Zeeman effect there is the quadrupole interaction for $I \geq 1/2$. The quadrupole interaction is described by the third term of the multi-pole Taylor expansion of the electrostatic energy potential. Details can be found in Refs. [1] and [2]. We write down the Hamiltonian, consisting of the Zeeman term $\mathcal{H}_z$ and the quadrupolar term $\mathcal{H}_Q$,

$$\mathcal{H} = \mathcal{H}_z + \mathcal{H}_Q = -\hbar\gamma\vec{I}(1+K)\vec{B}_0 + \frac{eQV_{zz}}{4I(2I-1)}\left[3I_z^2 - \vec{I}^2 + \frac{1}{2}\eta(I_+^2 + I_-^2)\right] \; . \qquad (2.25)$$

The first term contains also a magnetic shift K, which arises from the magnetic coupling of the electrons with the nucleus. This shift either originates form the motion of the electrons or from the magnetic moment associated with the electron spin. The former gives rise to the so called chemical shifts; the latter to the Knight shift in metals and to a coupling between nuclear spins.

In the quadrupolar term $I_+ = I_x + I_y$ is the raising and $I_- = I_x - I_y$ the lowering operator. eQ represents the quadrupole moment of the nucleus and Q the quadrupole tensor, which describes the deviation of the charge distribution of the nucleus form the spherical symmetry. The EFG tensor $V_{ij} = \frac{\delta^2 V}{\delta x_i \delta x_j}$ can be described by choosing the principal axis system with the convention $|V_{xx}| \leq |V_{yy}| \leq |V_{zz}|$ and using the asymmetry parameter $\eta = \frac{V_{xx} - V_{yy}}{V_{zz}}$.

The effect of the Zeeman and the quadrupole interaction for a spin $I = 3/2$ nucleus is illustrated in figure 2.2. By treating the quadrupole Hamiltonian as a perturbation, the values of the energy levels can be computed analytically (see Refs. [1] and [3]).

2.4.1 First-order quadrupole effect

For axial ($\eta = 0$) symmetry of the EFG the transition frequency is given by

$$\nu(m \leftrightarrow m - 1) = \nu_L + \frac{1}{2}\nu_Q\left(3\mu^2 - 1\right)(m - 1/2) \qquad (2.26)$$

with $\mu = \cos\theta$ and θ the angle between the z-axis and the applied external magnetic field $\vec{B}_0$ [3]. The quadrupole frequency ν_Q is defined as

$$\nu_Q = \frac{3eV_{zz}Q}{2I(2I-1)h} \; . \qquad (2.27)$$

We observe that the $(\frac{1}{2} \leftrightarrow -\frac{1}{2})$ transition is not affected by the first order quadrupole effect. All other transitions are shifted in frequency resulting in satellites in the Fourier spectrum (see figure 2.2). This way we get $2I$ different lines.

In the case of a powder sample consisting of many small crystallites oriented randomly, the resonance lines broaden. To calculate the line shape, the contributions from all spatial
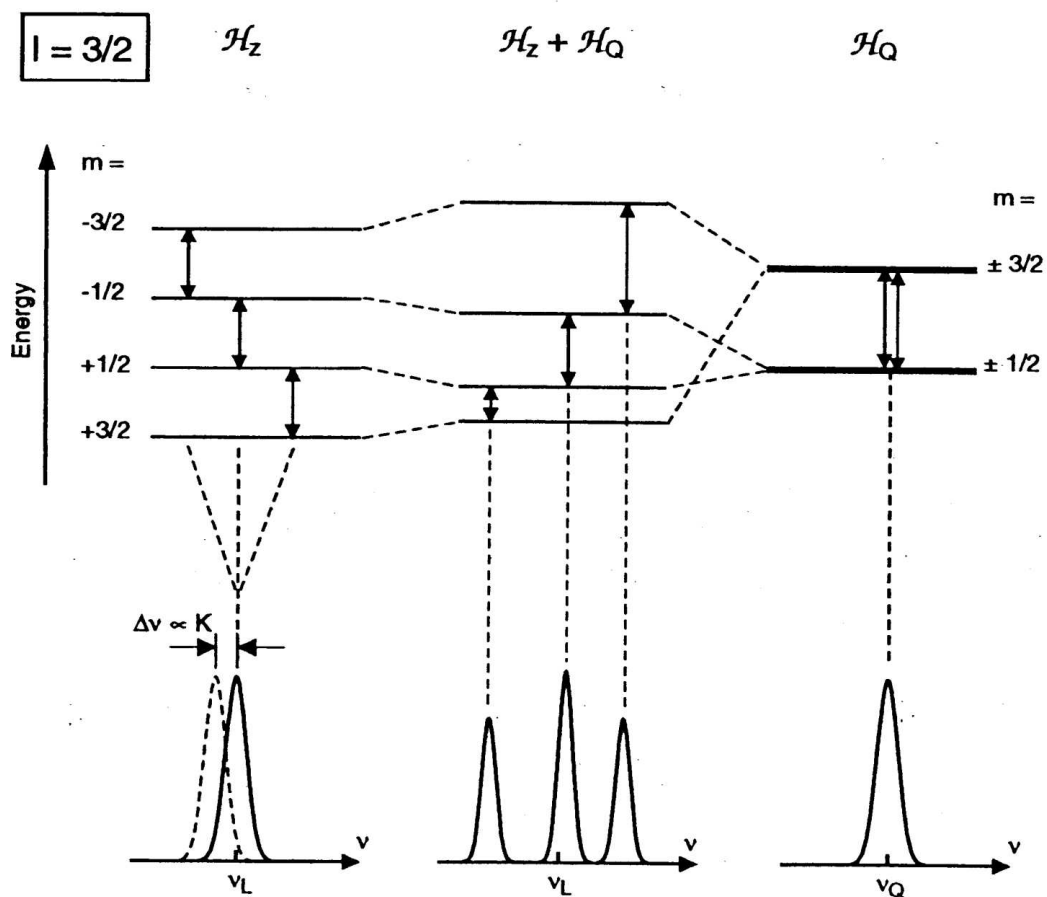
Figure 2.2: Result of the combination of the Zeeman and the quadrupole interaction for a Spin $I = 3/2$ nuclei in an external magnetic field.

orientations have to be included via powder averaging. The theoretical frequency pattern of a powder sample for a spin $I = 7/2$ nuclei is displayed in figure 2.3. In powder samples ν_Q represents the splitting of the first pair of peaks, half the splitting between the following pairs of peaks, etc. (see figure 2.3).
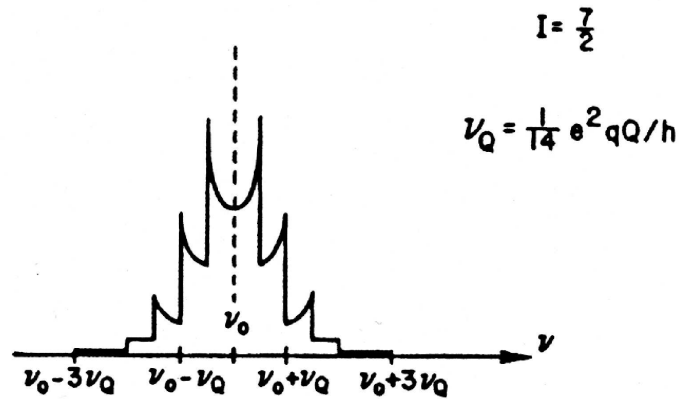
Figure 2.3: NMR quadrupole spectra for a Spin $I = 7/2$ nuclei. Six peaks can be seen. The central peak ($\frac{1}{2} \leftrightarrow -\frac{1}{2}$) is represented by the dashed line. ν_0 is the position of the central line and can be shifted compared to ν_L. [3]

An additional first-order broadening occurs if there are imperfections in the lattice, such as dislocations, strains, vacancies, interstitial, foreign atoms, etc. The EFG varying not only in orientation but also in magnitude from site to site, has a considerable influence on the shape of the resonance lines. In some cases the satellites will be completely wiped out by first-order quadrupole broadening, whereas the central line ($\frac{1}{2} \leftrightarrow -\frac{1}{2}$) will be practically unaffected. A single resonance line will then be observed and the quadrupole broadening will manifest itself only through the loss in intensity.

2.4.2 Second-order quadrupole effects

For axial symmetry the second-order transition frequency for a single crystal is given by:

$$
\begin{aligned}
\nu(m \leftrightarrow m-1) \;=\; & \nu_L + \frac{1}{2}\nu_Q\left(3\mu^2-1\right)(m-1/2) + \frac{\nu_Q^2}{3\nu_L}(1-\mu^2) \\
\times\; & \{[102m(m-1) - 18I(I+1) + 39]\mu^2 \\
-\; & [6m(m-1) - 2I(I+1) + 3]\} \; .
\end{aligned}
\tag{2.28}
$$

This induces a shift of the central line. By defining $\nu_{\frac{1}{2}}$ as the frequency of the central line, which is also called the center of gravity, the shift can be described in the case of a powder sample by taking the difference [3]

$$
\nu_L - \nu_{\frac{1}{2}} = \frac{8}{15} \cdot \frac{\nu_Q^2}{\nu_L} \cdot \frac{1}{64}(2I-1)\cdot(2I+3) \; .
\tag{2.29}
$$

The shift of the central line to lower frequencies is proportional to $1/\nu_L$ and becomes negligible for high magnetic fields. The satellites are also shifted with respect to ν_L. With weak second-order quadrupole interaction the satellites are not noticeably affected, but when the second order effects become stronger, the satellites shift by different amounts from their first-order positions. In extreme cases, this causes the satellites to change to different relative positions [3]. Pairwise ($\pm\frac{3}{2} \leftrightarrow \pm\frac{1}{2}$, $\pm\frac{5}{2} \leftrightarrow \pm\frac{3}{2}$, etc.) their separation remains the same. The shape of the central line of a powder sample is also influenced, it becomes asymmetric and a splitting can be observed (figure 2.4).
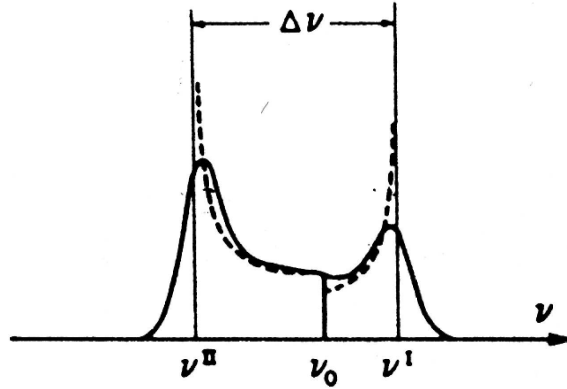
Figure 2.4: Spectrum for the central line ($\frac{1}{2} \leftrightarrow -\frac{1}{2}$) with second-order quadrupole effects present. The dashed line represents the theoretical function while the solid line is a symmetrically broadened shape. The frequencies ν^I and ν^{II} correspond to μ values of 0 and $\sqrt{5/9}$ respectively. [3]

The shape is determined by different shifts due to the different angles θ of the randomly oriented powder crystallites. Considering figure 2.4 the right maxima occurs at $\mu = 0$

$(\theta = 90°)$, with the frequency

$$\nu^I = \nu_L + \frac{\nu_Q^2}{16\nu_L}[I(I+1) - 3/4] \ .$$ (2.30)

The left maxima is at $\mu = \sqrt{5/9}$ ($\theta = 41.8°$) with the frequency

$$\nu^{II} = \nu_L - \frac{\nu_Q^2}{9\nu_L}[I(I+1) - 3/4] \ .$$ (2.31)

The difference between the two maxima is

$$\Delta\nu = \nu^I - \nu^{II} = \frac{25\nu_Q^2}{144\nu_L}[I(I+1) - 3/4] \ .$$ (2.32)

If the second-order quadrupole interaction dominates the shape of the line, the central-line width varies inversely with the Larmor frequency. An additional second-order broadening arises from by imperfections of the crystallites, similar to the ones discussed in subsection 2.4.1.

Chapter 3

Experimental Apparatus

In this chapter the experimental apparatus is introduced. At first there will be a schematical overview of the instrumental part of NMR and then the different components are described. Continuing with a presentation of the *Physical Properties Measurement System* PPMS, manufactured by Quantum Design, we will advance to the combination of this two systems. The home made NMR components, the 70 MHz spectrometer and NMR probe head will be discussed in separate chapters for deeper consideration.

3.1   Schematical description

The following description refers to figure 3.1. The pulse generator creates rectangular pulses, whose lengths t_p can be set to a desired valued. Several pulses in a row can be generated, whose time spaces are controlled by the pulse card. In the software the repetition time t_{rep} of a pulse sequence and the spacing time τ between the pulses of a package are set. Typical timescales are μs for a pulse, some ms for the spacing time, and fractions of a second to several seconds for the repetition time. The spectrometer allows a high-frequency AC signal pass coming from the frequency generator during a chosen pulse length. This signal has an amplitude that is too large for the broad-band power amplifier and is therefore attenuated.

Due to the slow response of the power amplifier a gate-delay is set in between. It activates the power amplifier and delays the pulse command to the spectrometer to switch into the transmitting mode for sending a pulse. This amplified package is guided through the duplexer to the probe head. There, in the resonance circuit which consists mainly of two capacitors and a coil, the pulse excites an oscillating magnetic field in the coil. The resonance circuit will be explained in more detail in the NMR probe head construction section 4.1.3.

After the excitation, the whole system switches to the receiving mode. The weak outcoming signal is driven by the duplexer into the receiver path, beginning with the pream-
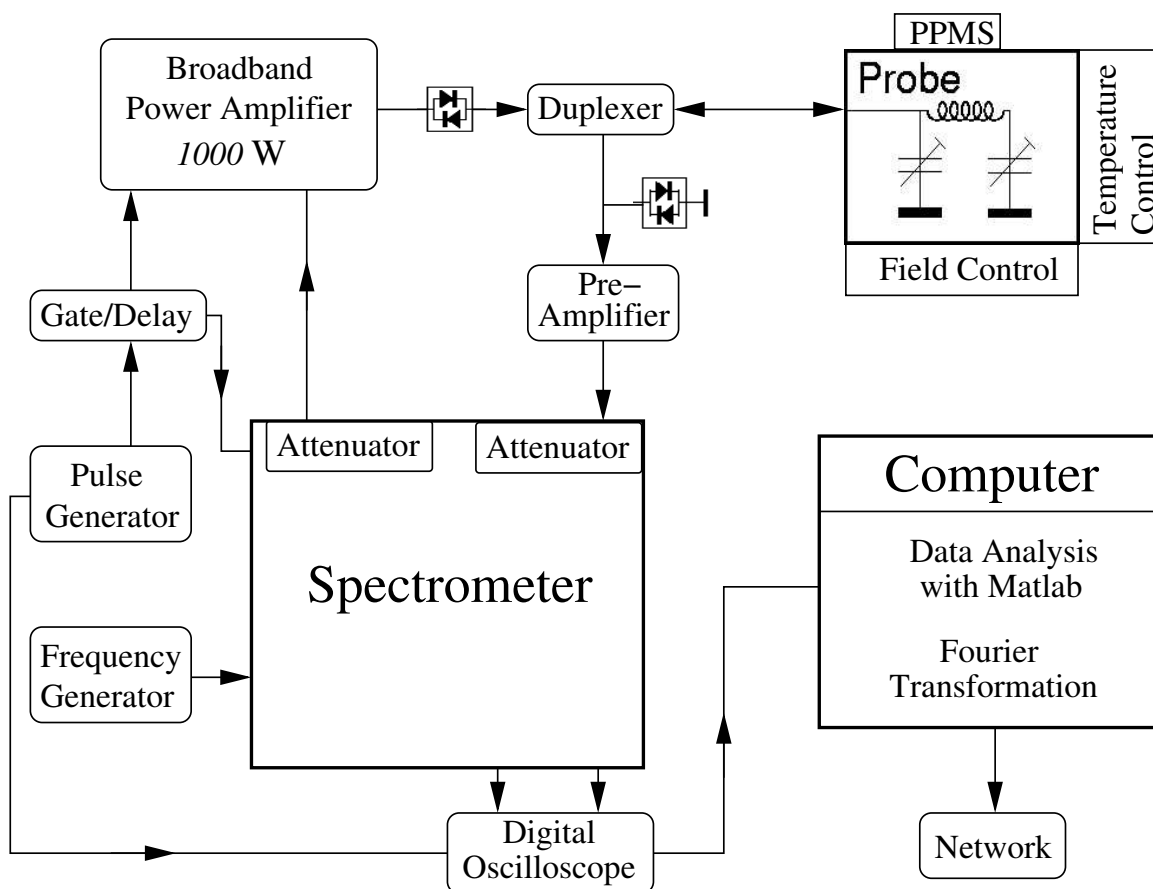
Figure 3.1: Schematical description of the NMR apparatus.

plifier for intensification. The receiving attenuation is used to prevent an overload of the spectrometer. The spectrometer transforms the complex signal into two parts with a phase difference of 90° and sends them to the digital memory oscilloscope. At this point the chosen amount of sweeps is saved in the buffer, summed up, and the mean value is displayed. This way it is possible to considerably improve the signal-to-noise ratio. The oscilloscope is triggered by the pulse controller. The processed complex signal is taken out through the IEEE-interface into the computer and it is converted into a Matlab-variable in matrix form and saved for further analysis.

3.2 NMR components

In this section the different used NMR components will be described. A picture of the NMR apparatus is shown in figure 3.2
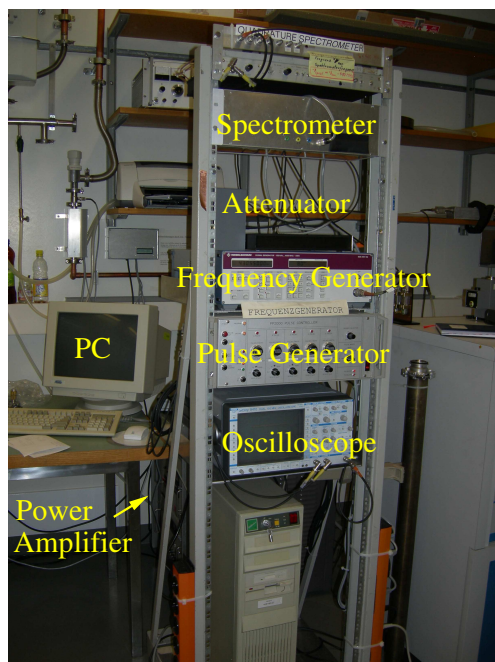
Figure 3.2: Wrack holding units of the NMR Apparatus.

Frequency generator: (*Rohde & Schwarz*; Model: *Signal Generator 100 kHz . . . 1000 MHz SMG*) & (*PTS*; Model: *PTS 310, Frequency Synthesizer 1-310 MHz*)**:**
It creates the frequency signal for the spectrometer. The *radio frequency* (RF) to be set is the sum of the spectrometer's internal working frequency and the chosen frequency ν_s for the experiment. It also produces the reference frequency of 10 MHz for the spectrometer.

Pulse generator: (*University of Zürich: H. Zimmermann, L.Pauli*; Model: *PP2000 Pulse Controller*)**:**
The pulse lengths t_p are set with the pulse generator. Pulses of 0.5 μs up to 10 ms are available. Five pulses can be created whereas the order of the pulses must be set. One of those pulses is used as a trigger for the oscilloscope. The timing of these pulses is controlled through the PP2000 parallel processor pulse card[3.1] and is controlled by the software.

Oscilloscope: (*LeCroy*; Model: *LeCroy 9410 Dual 150 MHz Oscilloscope*)**:**
The received complex signal is shown on the screen, temporarily saved in the memory,

---

[3.1]For more information check Ref. [16].

and its average is calculated. Up to one million entries can be summed. Over the IEEE-Port the complex data is passed to the computer.

Attenuator: (*Trilithic*; Model: *BMA-580*)**:**
Is used to attenuate the transmitted signal before the power amplifier. In the 70 MHz spectrometer this is done internally (see section 4.2.1). With the Lupotto IV spectrometer we use the following device, which is able to attenuate up to 80 dB:

Wideband power amplifier: (*Kalmus*; Model: *Wideband Pulse Amplifier LP1000LRF, 1000 Watt, 5-160 MHz, 61 dB Gain*)**:**
The pulse package is strongly amplified, and is given forward through the duplexer to the probe head. Because of the amplifier's slow response the gate/delay is set before the amplifier.

Gate/Delay: (*NMR-Team, Physics Institute, University of Zürich*)**:**
When the gate receives a pulse from the pulse generator, it sends a TTL signal to the power amplifier to get it activated. After an adjustable delay the pulse is sent to the spectrometer.

Duplexer: (*NMR-Team, Physics Institute, University of Zürich*; Model: *30-76 MHz*) & (*NMR-Team, Physics Institute, University of Zürich*; Model: *15-30 MHz*)**:**
The signal from the power amplifier is guided to the probe head. The returning spin signal is directed to the preamplifier. To prevent the power amplifier to feed noise through the duplexer when no pulse is to be sent, antiparallel diodes in series are set before the duplexer. Only AC voltages higher than 0.6 V can pass.

Preamplifier: (*MITEQ*; Model: *AU-1448*)**:**
Amplifies the weak spin signal and sends it to the spectrometer. The amplification is of 53.5 dB according to the constructors data sheet. Antiparallel diodes are set to the ground before the preamplifier to prevent damage on it through extruding remnants of the pulse. This way voltages over 0.6 V are absorbed.

Software: The software runs on Matlab on a Windows 3.1 operating system[3.2]. We used mainly 3 types of Matlab function scripts (M-Files).

pppc stands for *pulse programming for personal computer*. It is an interface to control the repetition time t_{rep}, the spacing time τ, the number of sweeps, the phase changes, and the toggle mode. It is very useful to get started and for optimization of the pulses.

[3.2]The reason of using this older computer is the incompatibility of the pulse card with newer computers and operating systems.

t2seq14 is a Matlab function script to make T_2 echo measurements and it is a useful tool to obtain clean echo signals. In the command the name of the output file, the amount of sweeps, the spacing time τ, and the repetition time t_{rep} are set. t2seq14 consists of two measurement series making a different pulse-phase interplay to reduce instrumental noise produced by the pulses. Afterwards the difference between these two measurements is taken with the Matlab function-script pp_pcdif to eliminate an overall offset. Each of these measurement series carries out the given amount of sweeps.

t2seq14 is also used in the fldscan1 function.

fldscan1 is a function to combine the NMR apparatus with the PPMS. This function is described in more detail in section 3.4.

Spectrometer: Two spectrometers were used, the self made 70 MHz spectrometer and the Lupotto IV spectrometer. The 70 MHz spectrometer is described in section 4.2.1. For comparison the Lupotto IV spectrometer is described in the following subsection.

3.2.1 Lupotto VI spectrometer

The Lupotto IV spectrometer was built for the Institute of Physics (University of Zürich) by P. Lupotto. It is the fourth and last one of the Lupotto series. The spectrometer was complemented later on, documented and repaired on various occasions by P. Soland at the same institute.

To describe the spectrometer we will follow the sketch shown in figure 3.3 on page 20. The spectrometer's internal working frequency is 410 MHz. The incoming frequency generator (*frequency synthesizer*) signal[3.3] is the sum of the working frequency and the chosen frequency $F = \nu_s$ used for the experiment. Parallel to it the spectrometer receives the reference frequency of 10 MHz from the frequency generator. This frequency is transformed by the *harmonic generator* into a 390 MHz and a 80 MHz signal. The 80 MHz signal is split by the *4-phase modulator* into four 20 MHz signals with four different phases (0°, 90°, 180°, and 270°). The 20 MHz signal with the chosen phase is mixed in *conversion 2 transmitting* with the 390 MHz one to continue with a 410 MHz signal with the chosen phase.

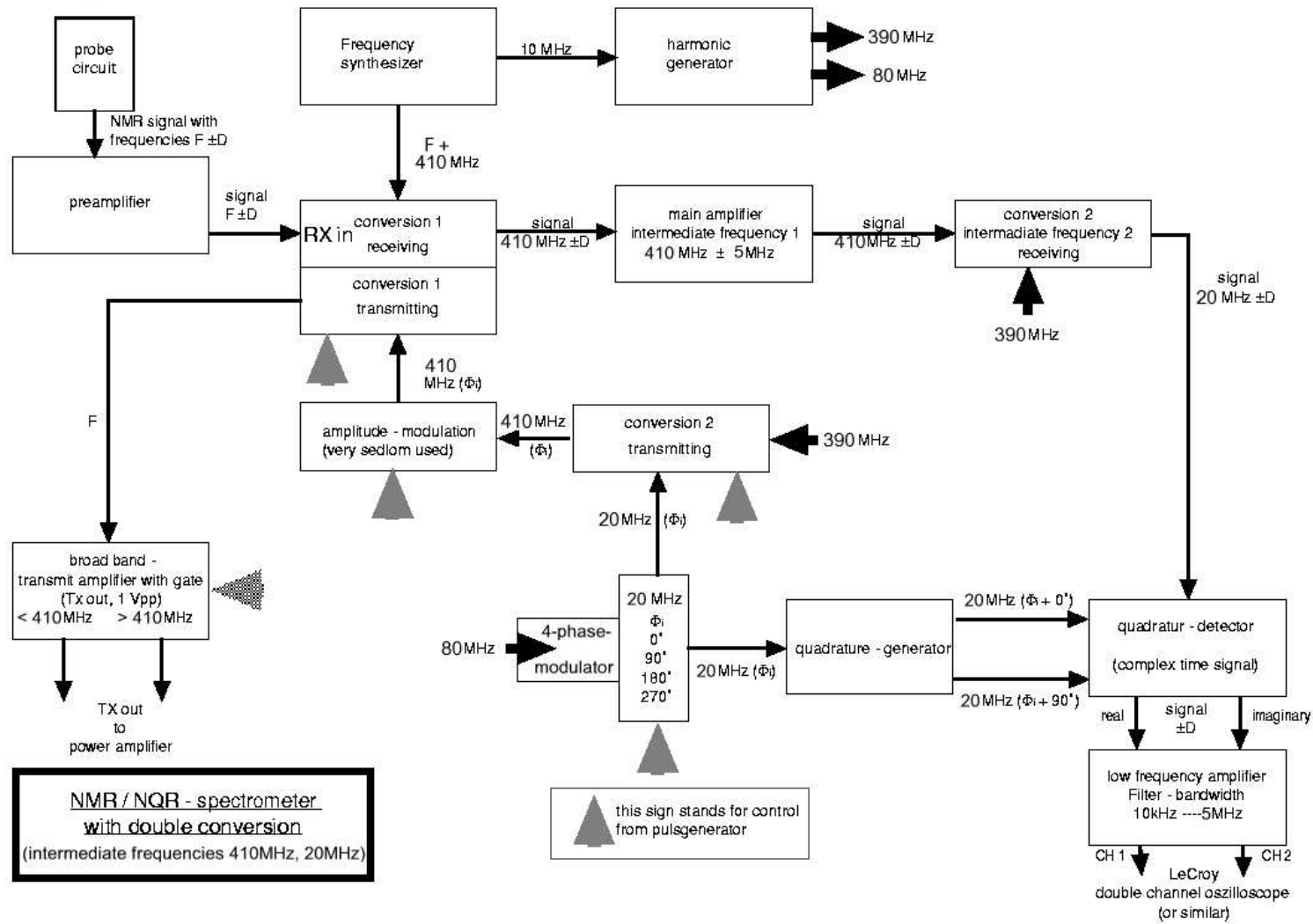---

[3.3]Connector: *Lo IN*

Figure 3.3: Schematical description of the Lupotto IV spectrometer.

The conversion units are mixers working as multipliers with two output signals, where the unwanted ones are filtered out. For more clarity we resume the conversion units in table 3.1.

conversion element	input 1	input 2	wanted output	unwanted output
conv. 1 transmitting	$F + 410\,\text{MHz}$	$410\,\text{MHz}$	F	$F + 820\,\text{MHz}$
conv. 2 transmitting	$390\,\text{MHz}$	$20\,\text{MHz}$	$410\,\text{MHz}$	$370\,\text{MHz}$
conv. 1 receiving	$F + 410\,\text{MHz}$	$F \pm D$	$410\,\text{MHz} \pm D$	$410\,\text{MHz} + 2\cdot F \pm D$
conv. 2 receiving	$410\,\text{MHz} \pm D$	$390\,\text{MHz}$	$20\,\text{MHz} \pm D$	$800\,\text{MHz} \pm D$

Table 3.1: Summary of conversion elements used in the Lupotto IV spectrometer.

This 410 MHz signal is mixed in *conversion 1 transmitting* with the input signal coming from the frequency generator. What remains is the chosen frequency F that is passed to the power amplifier[3.4] during the pulse time, which is set by the pulse controller.

The spin signal returning from the experiment[3.5] is the chosen frequency F with an added frequency window $\pm D$. In *conversion 1 receiving* the spin signal is mixed with the frequency generator signal yielding the signal at $410\,\text{MHz} \pm D$. The *main amplifier* amplifies a window of $410\,\text{MHz} \pm 5\,\text{MHz}$. In *conversion 2 receiving* the main amplifier output is mixed with the 390 MHz signal. The resulting $20\,\text{MHz} \pm D$ signal is split in the *quadrature detector* into two by 90° phase shifted parts, which can be interpreted as the real and imaginary part of a complex signal $0\,\text{MHz} \pm D$. This splitting is achieved through a mixing with two 20 MHz signals from the *quadrature generator*, which differ by 90° in phase. The *quadrature generator* receives the phase dependent 20 MHz signal from the *4-phase-modulator*. This phase is also adjustable. The resulting signal $0\,\text{MHz} \pm D$ is passed to the oscilloscope.

[3.4]Connector: *Tx OUT*
[3.5]Connector: *Rx IN*

3.3   PPMS: A short description

The *physical properties measurement system* (PPMS), a device manufactured by Quantum Design, is an open architecture, variable temperature-field system which allows automated measurements for physical properties such as heat capacity, magnetization, magnetic torque, Hall-effect, DC resistivity, and other thermal and electronic properties of a sample. The magnetic field can be set up to $9\,\mathrm{T}$, and the temperature covers a range from $1.8 - 400\,\mathrm{K}$, or down to $0.4\,\mathrm{K}$ with a Helium-3 refrigerator. The possibility of easily controlling the field and the temperature, makes the PPMS an interesting option for doing NMR measurements. We restrict this PPMS description to the used features and specifications, such as the field and temperature controlling, the automation of the system, and the sample space dimensions. For all other features and specifications we refer to Refs. [4] and [5].

A picture of the PPMS is shown in figure 3.4. The system can be completely controlled and monitored through the model 6000 controller or the MultiVu software running on a PC. Easy sequence script can be written with the MultiVu software to let the PPMS work fully automated. Unfortunately this MultiVu software is not as easy to use for communication with external devices since the standard IEEE communication protocols are not directly supported.

Figure 3.4: PPMS and Model 6000 Controller.

The *high-capacity nitrogen jacked dewar* [4] prevents fast liquid helium boil-off. The PPMS insert (figure 3.5) with the superconducting magnet is immersed in liquid helium. The outer layer of the insert is a superconducting magnet, which is made of NbTi/Nb$_3$Sn. The superconducting coil can be charged and discharged[3.6] using the persistent switch. After charging, the magnet is set to persistent mode, i.e. disconnected from its power supply.

There are three modes for setting the magnetic field: The oscillating mode, the no-overshooting mode and the linear mode. As shown in section 5.1.4 the oscillating mode is almost stable, while the other modes result in a drift of the field[3.7]. The field uniformity is claimed to $\pm 0.01\%$ over a $5.5\,\text{cm} \times 1\,\text{cm}$ cylindrical volume with the center at $5.1\,\text{cm}$ above the puck surface. This has been verified in the testing phase of the NMR probe head (section 5.1.2).

For temperature control the PPMS offers the *high-temperature control* and the *continuous low-temperature control* techniques [4], which allow a fast cooling and heating of the PPMS sample space[3.8], a smooth transition through the $4.2\,\text{K}$ helium boiling point and maintain indefinitely a temperature below $4.2\,\text{K}$. Thermal control and monitoring is situated below the PPMS sample puck. To monitor and control thermal gradients in the PPMS sample space, a neck thermometer and heater is wrapped around the sample at about $14\,\text{cm}$ above the puck surface.
For additional information we refer to the PPMS User's Manual, see Refs. [4], [5] and [6].

[3.6]This with a maximal charging rate of $196.3\,\text{Oe/s}$

[3.7]We tested linear mode only.

[3.8]Typical warming and cooling rates are around $6\,\text{K/min}$, although they can be extended and set up to $20\,\text{K/min}$.
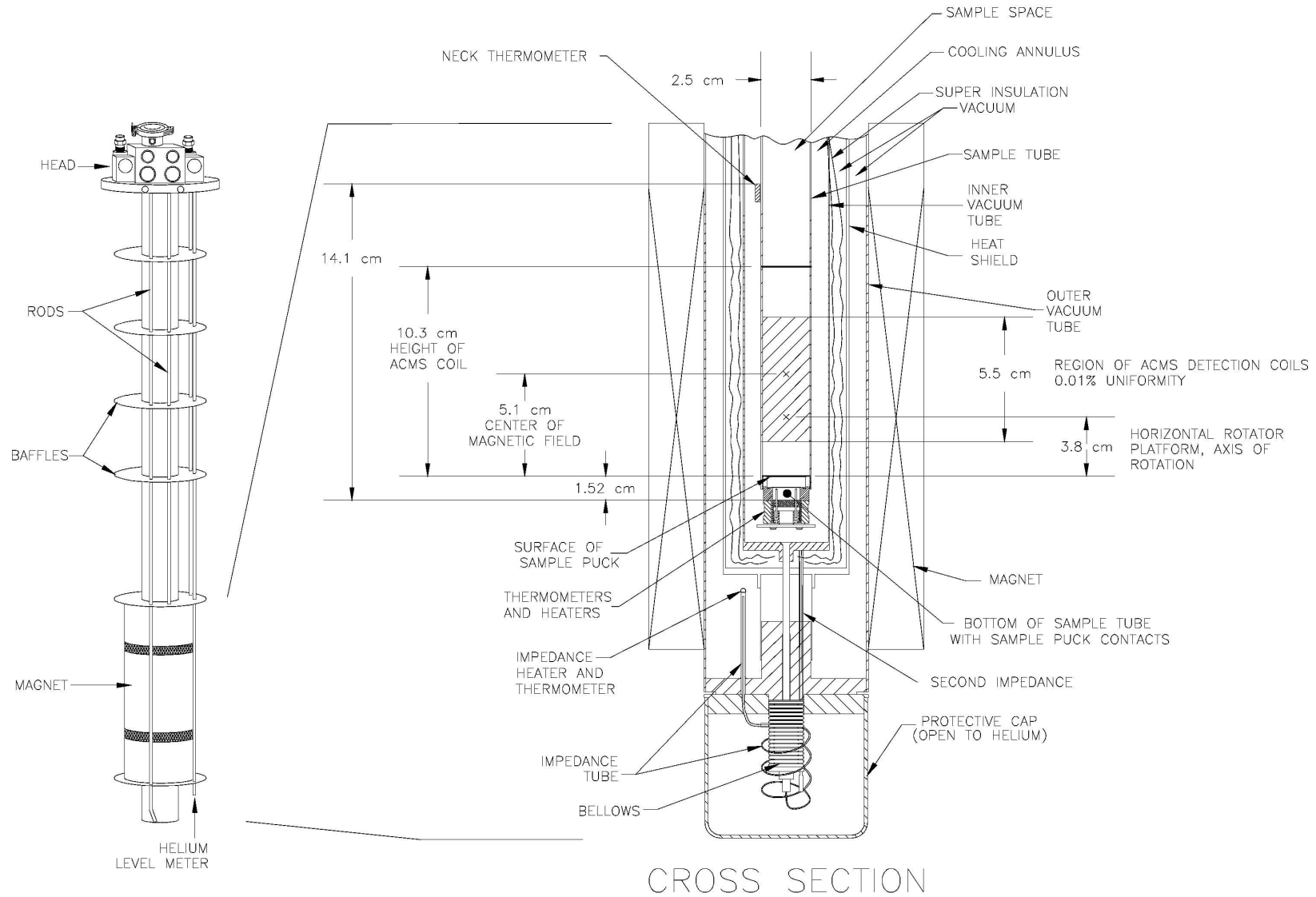
Figure 3.5: Schematical overview of the PPMS insert head and sample space. [4]

3.4 Combining the NMR apparatus with the PPMS

In this chapter we will discuss how the NMR was combined with the PPMS. Because of the automated characteristics of the PPMS, it would be plausible to use the MultiVu software for this purpose. However there are several arguments against this option. Although the PPMS software offers many possibilities for control and calibration purposes, it is rather difficult to integrate external hardware and software. The most common way would be to use LabVIEW. To control the NMR-apparatus, however, we would have to rewrite and adapt many parameters. Moreover, we would have to expect severe compatibility problems because the NMR pulse card is running in an old Windows 3.1 environment. So we decided to drive the PPMS with the PC of the NMR-apparatus.

To do so the MultiVu software was not used at all, and the controlling of the PPMS was done by direct connection through the *general purpose interface bus* GPIB port to the *Model 6000 Controller*. As the NMR apparatus is controlled with Matlab, there is also the possibility to drive the PPMS system with basic Matlab GPIB commands.
For this purpose the `fldscan1.m` function was written, which we will overview in the following. We will point out the most important script commands and GPIB commands. The whole program code is presented in appendix A.
The function to run a field scan is defined as follows:

```
fldscan1(name,f_begin,f_step,f_end,query);
```

The parameters to be set are:

name: The name of the data file must be chosen and set as a string variable. The variables `mes_dat`, `echointens`, `cernox_Resist` and `ppms_temperature` will be saved into a MAT-File with this name.

f_begin: Initial magnetic field value in Oersted.

f_step: Magnetic field stepping size in Oersted.

f_end: Final magnetic field value in Oersted.

query: Setting the NMR parameters. By setting query $= 1$ the user will be asked to set the values for the NMR parameters. If the query is set $= 0$ or else, the values have to be set directly in the `fldscan1.m` file.
The NMR parameters are: The spacing time `tau`, the repetition time `RR`, the number of sweeps `sweeps`, the size of the baseline correction window `bc_window`, and the integration limits over the echo `i_left` and `i_right`, respectively.

The output variables `ppms_temperature` and `cernox_Resist` are vectors with one readout per magnetic field point. `echointens` is a 2 column matrix, containing in the first column the magnetic field points and in the second one the integral over the echo (section 2.3.1), which represents the intensity of the signal at a given field as a complex number. The

values are drawn in a figure window which allows online inspection while the experiment is running. `mes_dat` is a so called format-1 matrix (see NMR Matlab description).

In the following we describe the sequence of commands of the script `fldscan1.m` (appendix A). First the function is defined. After some comments the relevant NMR parameters are specified. Then the figure is plotted and the variables and the GPIB port are initialized. At that point the main `for`-loop which runs the experiment starts.
At first the magnetic field is set with the following command:

```
sendgpib(15,['FIELD ' f_str ' 100 2;']);
```

The `sendgpib`, like the `readgpib` command, are Matlab commands in order to connect to other machines through the GPIB port. The first value has to be the GPIB port number of the machine, which is in our case `15`. The second expression is expected to be the string command to manipulate the machine by applying the language of the machines. For this purpose Quantum Design offers a chapter in the software manual called "PPMS GPIB Commands Manual" in Ref. [5].
The GPIB string command to set the field looks as follows:

```
FIELD Field Rate [ApproachMode] [MagnetMode];
```

The `Field` has to be set in Oe, the `Rate` defines the field setting speed (in Oe/s). Then the optional parameters follow. The `ApproachMode` is `0` for default *Linear Approach* mode, `1` is for *No-Overshoot Approach* mode and `2` for *Oscillating Approach* mode which is used by us because of the smaller drift of the magnetic field as will be described in section 5.1.4. The `MagnetMode` is set to `0` for *Persistent Mode* (default, also in all our experiments) and `1` for *Driven Mode*. Each string command for the *Model 6000 Controller* has to end with a semicolon[3.9].

Next a while loop had to be inserted to wait for the PPMS to set the field and turn into the *Persistent Mode*. To do so the PPMS is asked periodically for the status. This is done with the `readgpib` command, containing the string command:

```
GETDAT? DataFlag [NoUpdateFlag];
```

In `DataFlag` the data strings to be returned have to be chosen. This is done by setting a 32-bit integer which is, chosen according to the list in appendix A of the "PPMS GPIB Commands Manual" [5]. To read out the status, we set `1`, which gives us first the time stamp of the PPMS ending with a comma, followed by the PPMS status, and finally a semicolon. The status is a four digit hexadecimal number. The first digit is the temperature status, the second the magnet status, the third the chamber status and the last the sample position. This is also described in the appendix of the "PPMS GPIB Commands Manual" [5]. In our case we are looking for a magnet status $= 1$. The default optional

---

[3.9]Not described in Ref [5].

`NoUpdateFlag` is by default `0` for updating all readings before returning the data, and `1` for returning the most current values immediately. We use the default. To read out these data, some skills had to be applied in order to turn strings into integers to select the right output values to be treated.

The field value, the temperature and the resistance of the cernox thermometer are read out. For this the same `GETDAT?` GPIB command is used, but with a `DataFlag` value of 22 to read out the desired value.

The NMR measurement starts at the set magnetic field. For this we use the scripts `t2seq14` and `pp_pcdif`, which are explained in section 3.2. The echo intensity integral is evaluated with the `echoeval` command, which makes the baseline correction and the integration. Then the values are written into the variables which are saved and the scan data are drawn in the figure window. We also inserted in the `for`-loop the `tic` and `toc` command to have an idea how long the measurement at each field takes.

We have to emphasize that the NMR computer is unaccessible during the whole scan, the only way to have access to the data is by downloading the MAT-file (containing the measured values) to another computer.

Because of problems with the signal-to-noise ratio we used also the `fldscan2` function where the cernox resistance measurement is not included. The main goal of this step was to reduce the antenna effect of the connection leads to the cernox and prevent the PPMS to feed in extra noise through the user bridge.

To prevent quenching of the superconducting magnet due to a low helium level (below 60%) and reduce the helium consumption, a function script called `ppmsdown` was made. `ppmsdown` consists of a sequence setting the field to 0 Oe, waiting for the persist mode status on the magnet, and setting the temperature on standby modus with the `sendgpib` command `SHUTDOWN` [5].

Using `fldscan1` revealed a problem, mainly a Matlab problem, which concerns the filling of the virtual memory trough the storing of all variables during the whole scan (especially the variable `mes_dat`). At about 150 or 200 field points the computer is likely crash. For that reason it is recommendable to restart the computer in order to clear the virtual memory before starting a field scan. If there is a need to perform scans with more field points, we suggest to not use the `mes_dat` variable.

Chapter 4

Construction Part

The construction part of the NMR probe head and the 70 MHz spectrometer are the main subjects of this diploma thesis and its construction will be presented in this chapter.

4.1 NMR/NQR probe head

This section will motivate and present the construction of the NMR probe head, describe the environment to which it will be exposed, present the electrical system, and the temperature readout.

4.1.1 Motivation

There is a rich history of NMR/NQR studies on solid-state materials in the Physics Institute of the University of Zürich. In recent times this was especially driven forward by J. Roos and M. Mali, members of the Keller Group. The used experimental method, having a static field of about 9 T, is designed to perform frequency scans. The magnetic field of the superconducting magnet, produced by Cryomagnetics Inc., is very homogeneous and stable over years of usage. A sample can be cooled down to $\approx 7\,\mathrm{K}$.

With the PPMS magnet we can not reach such a high stability and homogeneity, but the possibility to have variable magnetic fields up to 9 T and to be able to cool the sample down to 1.8 K makes the PPMS a very interesting complementary option. Having a NMR/NQR probe for the PPMS would open various possibilities, such as performing magnetic field scans (in comparison to the used frequency scans) and to low temperature NMR or NQR.

4.1.2   Requirements for the probe head

Concerning the environment to which the probe head will be exposed, the choice of the material and the construction design had to be done with special care. Because of the high magnetic fields, the probe head had to be manufactured with low magnetic response materials, so that no mechanical forces are created and no inhomogeneity of the magnetic field is induced. Also, thermal conductance from the top of the sample space being at room temperature to the bottom with temperatures below the temperature of liquid helium at 4.2 K, over a distance of 89.3 cm had to be minimized. At the same time the probe head has to be mechanically stable and fit into the narrow tube of the sample space having a diameter of 2.68 cm.

In the following an overview of the used materials is given. The upper part of the probe head is mainly made of stainless steal (to achieve mechanical and thermal stability), with the exception of the capacitor driving mechanism, that is made partly out of aluminum (see figure 4.2). The used non-magnetic materials in lower part, extending 38 cm above the sample puck surface, are brass, Torlon[4.1] and Berilco[4.2] (see figure 4.4). The sample-coil holder and the sample plateau are made of Torlon.

4.1.3   Electrical properties of the probe head and the resonance circuit

This subsection has two parts: in the first part we describe the coaxial line down to the resonance circuit, in the second one we explain the resonance circuit that is used, with special focus on the tuning and matching capacitor.

The main purpose of the electrical system of the probe head is to deposit the major part of electrical energy as an oscillating magnetic field in the coil where the sample is placed. Moreover it is supposed to pick up the voltage, which is the response of the spinning nuclear magnetic moments. In order to avoid reflections the electric impedance of the resonance circuit has to match the impedance of the amplifiers, which have internal impedances of 50 Ω.

First of all a coaxial 50 Ω-line down to the circuit is crucial. It is also the main support of the probe head. We made the line of two stainless steal tubes with a lower part of brass. The outer tube has diameter dimensions of 6 and 5.5 mm, and the inner tube, which is kept centered with centering Teflon rings, has diameter dimensions of 2 and 1 mm. To calculate the characteristic wave impedance Z_L/Ω (in Ω) of the coaxial line we used a

---

[4.1]Torlon is a high-performance amorphous polyamide-imide polymer with exceptional mechanical and thermal properties.

[4.2]Berilco is a non-magnetic, thermal-stable copper-beryllium alloy.

common RF-technical formula [7]

$$Z_L/\Omega = \frac{60}{\sqrt{\varepsilon_r}} \ln \frac{D}{d} \; . \tag{4.1}$$

D is the inner diameter of the outer tube and d the outer diameter of the inner tube. By setting the dielectric constant for helium $\varepsilon_r(\text{He}) = 1.00007$ we get a characteristic wave impedance of $Z_L/\Omega = 60.7\,\Omega$ which is reduced by the Teflon centering rings ($\varepsilon_r(\text{Teflon}) = 2$) close to our expected $50\,\Omega$ impedance.
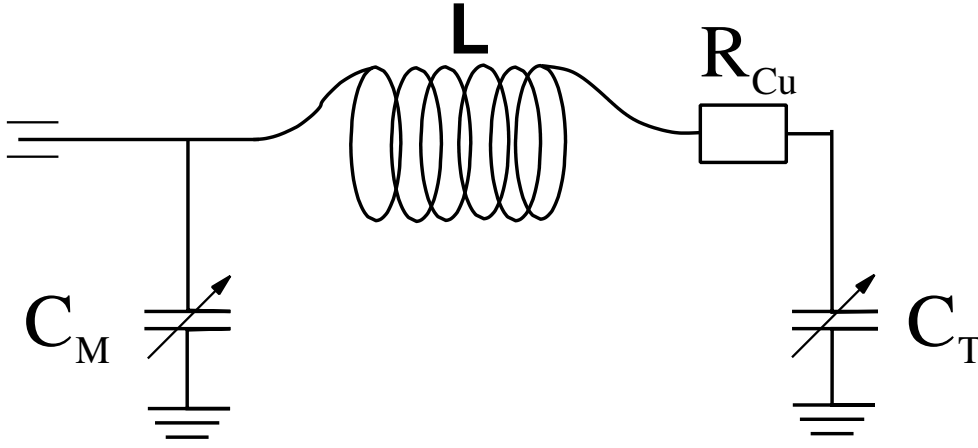

Figure 4.1: Schematical drawing of the resonance circuit.

Next we will discuss the resonance circuit shown in figure 4.1. The circuit consists of the coil L with an Ohmic resistance R_{Cu} and the tuning capacitor C_T in series. Parallel to both is the matching capacitor C_M.
The total serial impedance is

$$Z_{tot}^{serial} = i\omega L + \frac{1}{i\omega C_T} + R_{Cu} \; .$$

In order to achieve the resonance frequency $\omega = \omega_R$, $|Z_{tot}^{serial}|$ has to be minimal, i.e.

$$i\omega_R L + \frac{1}{i\omega_R C_T} = 0 \quad \Longrightarrow \quad \omega_R = \frac{1}{\sqrt{LC_T}} \; . \tag{4.2}$$

In resonance, $Z_{tot}^{serial} \approx R_{Cu} \approx 1\,\Omega$.
While the resonance frequency is manipulated by the tuning capacitor C_T, the parallel matching capacitor C_M adjusts the general impedance to $50\,\Omega$. C_M is a commercial capacitor with a range of $92\,\text{pF}$ up to $330\,\text{pF}$. Useful additional, experiment dependent options, are an additional capacitor C_{M_P} parallel to C_M to achieve the $50\,\Omega$ impedance, and a resistor R in between the coil and C_T to get a lower Q-factor and broaden the frequency range of the resonance cirquit.

The tuning capacitor C_T is a coaxial capacitor shown in figure 4.4. It consists of a Berilco tube soldered to the ground, a rounded[4.3] brass pin in the inside connected to the coil and a dielectric tube made out of quartz glass that can be moved in and out of the capacitor. The range of capacitance can be calculated by using the formula for a coaxial capacitance

$$C_T = 2\pi\varepsilon_0\varepsilon_r\frac{l}{\ln(R_2/R_1)} \ , \tag{4.3}$$

with the permittivity constant $\varepsilon_0 = 8.85 \times 10^{-12}$ Cb/Vm, the dielectric constant[4.4] ε_r, the length of the capacitor $l \simeq 10$ cm, the outer wall of the brass pin $R_2 = 5.4$ mm and the inner wall of the Berilco tube $R_1 = 10$ mm. The resulting range of capacitance is of 7.8 pF with the quartz glass maximally pulled out and 28.8 pF with the quartz glass pushed in. The coil itself has to be made to match the desired parameters of the planned experiment.

4.1.4   Construction

While the existing NMR/NQR probe heads in the Physics Institute have a diameter of 5 cm and more, our new probe head had to be reduced to a diameter of 2.6 cm, which presented the main difficulty of the probe head design.
The parts were designed using the construction environment software AutoCAD and then converted to the more powerful construction software CATIA for easier adaptation to the workshop machines. Two analogous probe heads were produced.

In the following the different parts of the probe head will be explained. On the top of the probe head (figure 4.2) there is the driving mechanism for the capacitors. The quartz glass position for the tuning capacitor can be set by turning the screw head. This screwing results in a vertical up and down motion of the stainless steel rod[4.5] which is attached to the quartz glass. The matching capacitor is directly attached through a shaft (stainless steel rod) with its screwing head.
The top also contains a BNC-connector to the coaxial line described in the chapter above and two 4-pin Lemo connectors prepared for electrical connections to the sample space. The flange (stainless steel) had to be carefully sealed so that sufficient vacuum can be produced inside the PPMS sample space.

The probe head is shown in figure 4.3. The probe head is mechanically reinforced by the 50 Ω coaxial line and an additional tube. The thinner two shafts manipulate the capacitors and are therefore freely movable. Along the support five horizontal plate assist thermal insulation and support. The upper four plates are made out of stainless steel, the lowest one is made out of Berilco. Below this plate there are no more stainless steel parts.

[4.3]Avoids electrical breakdown.
[4.4]ε_r(quartzglass) = 3.7 and ε_r(He) = 1.00007.
[4.5]To reduce the thermal conductance this rod is actually a 2×1 mm tube.
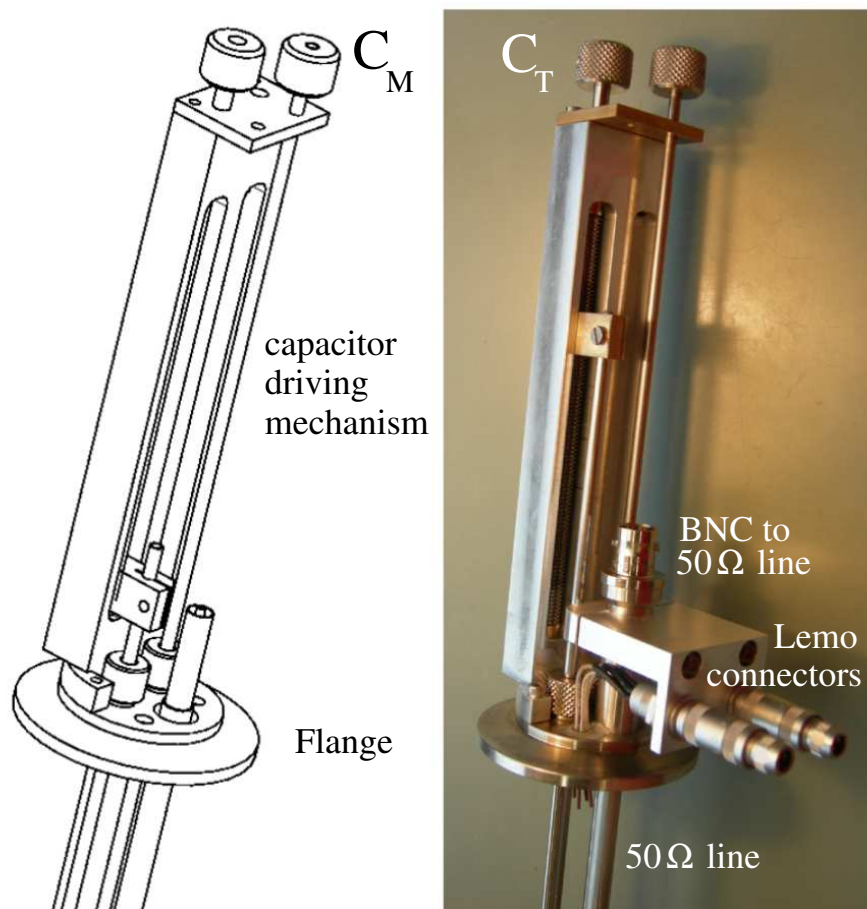
Figure 4.2: Top of the NMR probe head.

The capacitors are located at the bottom part (figure 4.4). The matching capacitor is screwed to the Berilco plate which is soldered to the tuning capacitor. In the sample space the inner coax line ends at the lower Berilco disk on which the three puck holding Berilco bars are attached to. The brass pin of the tuning capacitor is screwed into the Torlon plate. Three pins, the coax line pin, the tuning capacitor soldering pin, and the ground pin stick out below the Torlon disk. There are two open holes through the plates for the additional wires form the Lemo connectors. Three thin Berilco bars hold the puck plate, where the PPMS sample puck is attached to.

The sample plateau (figure 4.5) is out of Torlon and can be fixed with three small Berilco screws onto the bars. The coil-sample holder and the holder mounting are fastened on top of it with nylon screws. All these parts are made of Torlon. Two coil-sample holders of different sizes were made. The available standart Torlon sample capsules fit into the smaller of these coil-sample holders.
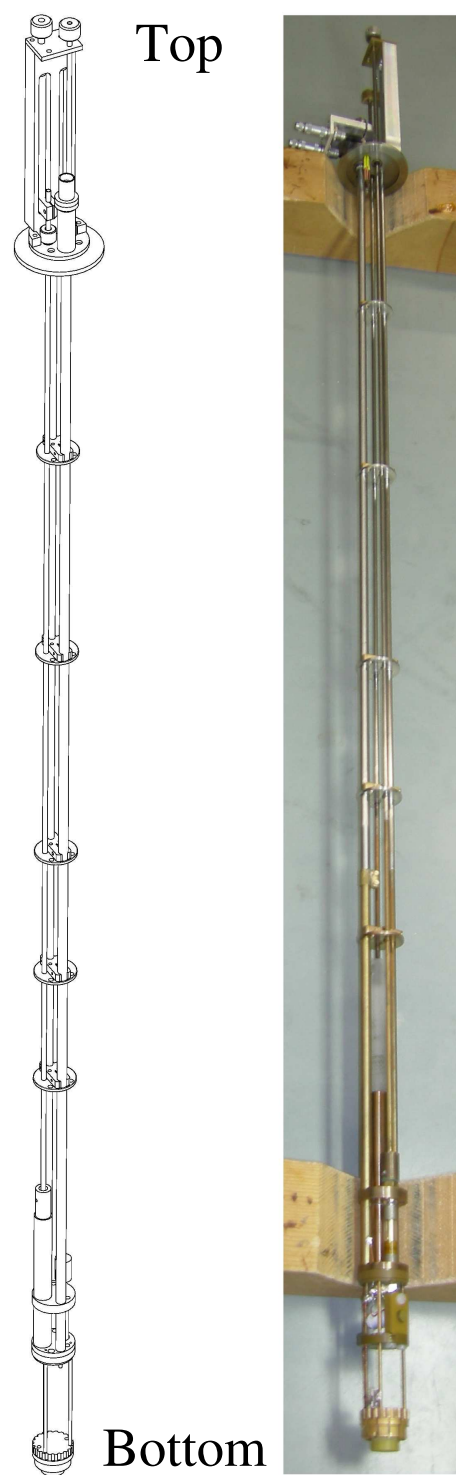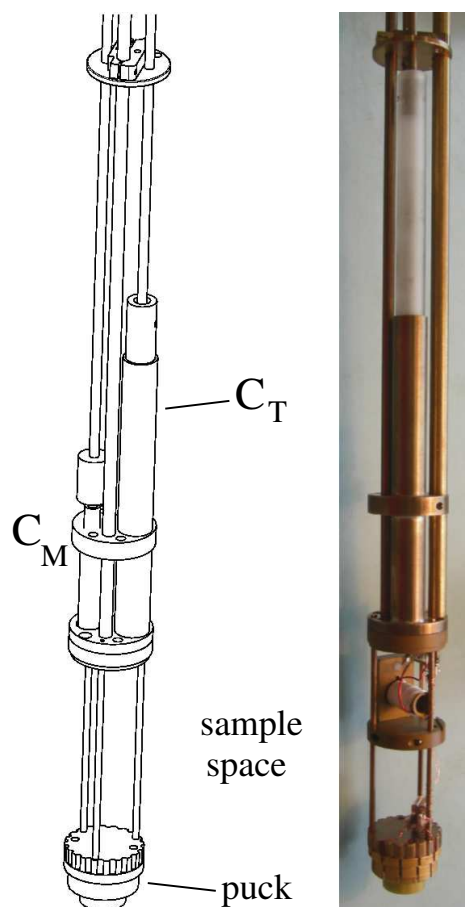
Figure 4.3: Full NMR probe head.

Figure 4.4: Bottom of the NMR probe head.
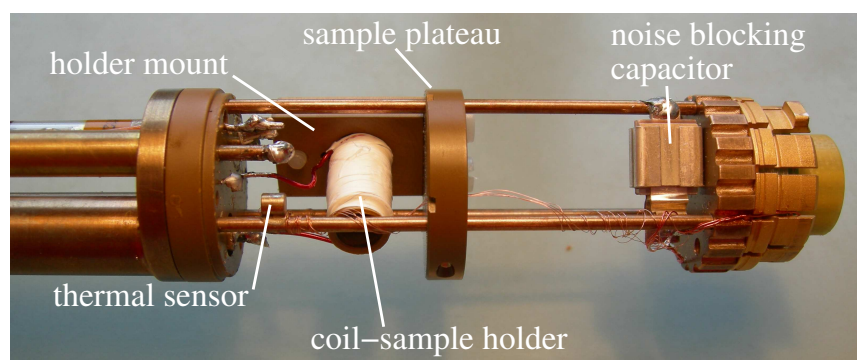
Figure 4.5: Coil-sample holder, plateau, thermal sensor, and sample puck.

4.1.5   Temperature readout

To have better control of the sample temperature, a *CERNOX* temperature sensor was installed close to the coil as seen in figure 4.5. The *CERNOX* sensor is read out through the *User Bridge 1* port by a 4-terminal measurement. The used connector pins on the puck are chosen according to a user Bridge resistance measurement using *Channel 1*, see the PPMS Hardware Manual [4].

The calibration measurements are carried out at $0\,\mathrm{T}$, $3\,\mathrm{T}$, $6\,\mathrm{T}$, $9\,\mathrm{T}$, and are presented in the appendix B[4.6].

Because of strong disturbing interference noise, two $1000\,\mathrm{pF}$ blocking capacitors were added.

[4.6]The data is saved on the PPMS computer in folder: `C:\QdPpms\Data\alex\cernoxCal`

4.2   70 MHz NMR spectrometer

In this section the construction of the 70 MHz spectrometer is described. The motivation of building a new spectrometer was that the previously used spectrometers, mainly the ones of the Lupotto series, are quite old and very complex. Moreover, RF elements are nowadays commercially available with good performance and at quite low costs. We copied the design of a similar spectrometer, which is used at the Solid State Physics Laboratory ETHZ [8], and adapted it to our needs.
Pictures of the 70 MHz spectrometer and its power supply are shown in figure 4.8.

4.2.1   Schematical description

The following description of the operating mode of the spectrometer refers to figure 4.6. The list of used elements can be found in appendix C.2. For a comparison with the Lupotto IV spectrometer we refer to section 3.2.1. The main difference between these two spectrometers, besides their internal working frequency, is that the new 70 MHz spectrometer has cannot handle RF-phases and is less powerful in amplification.

In standard operating mode (i.e. no pulse is to be sent) the spectrometer is in receive-mode. Once a pulse is sent, it switches to transmit-mode. How the TTL signal used to switch between this modes is generated is explained in the subsection below.

The transmitter signal is a mix of two incoming signals. The first signal from the frequency generator's 10 MHz reference is multiplied by 7 in the multiplier *(1)*, cleaned by the band pass *(2)* and switched *(3)* with a logical TTL 0 to the transmitter path. In mixer *(5)* this 70 MHz frequency is mixed with the second signal that is generated with the frequency generator, fed into the spectrometer through *Lo IN*, and switched on the transmitter path with switch *(12)*. This second signal is the chosen spectrometer frequency ν_s for the experiment, plus the 70 MHz internal working frequency of the spectrometer. The resulting signal from mixer *(5)* is at the chosen frequency ν_s. This signal is amplified in *(8)*, passed through by switch *(9)*, attenuated *(10)* with up to 65 dB and sent through *Tx OUT* to the power amplifier. Similar to the mixers used in the Lupotto IV spectrometer (section 3.2.1) we obtain two output signals, where the unwanted one is cleaned out with an external low pass filter *(11)*.

In the transmit-mode all switches have a logical 0, which means that the switches *(3)* and *(12)* are on transmit, switch *(9)* is feeding through and switch *(21)* is 50 Ω terminated. This state is the one shown in figure 4.6. For receive-mode all switches have a logical 1. Now the switches *(3)* and *(12)* are switched to the receiver path, switch *(9)* is 50 Ω terminated and switch *(21)* feeds the signal through.
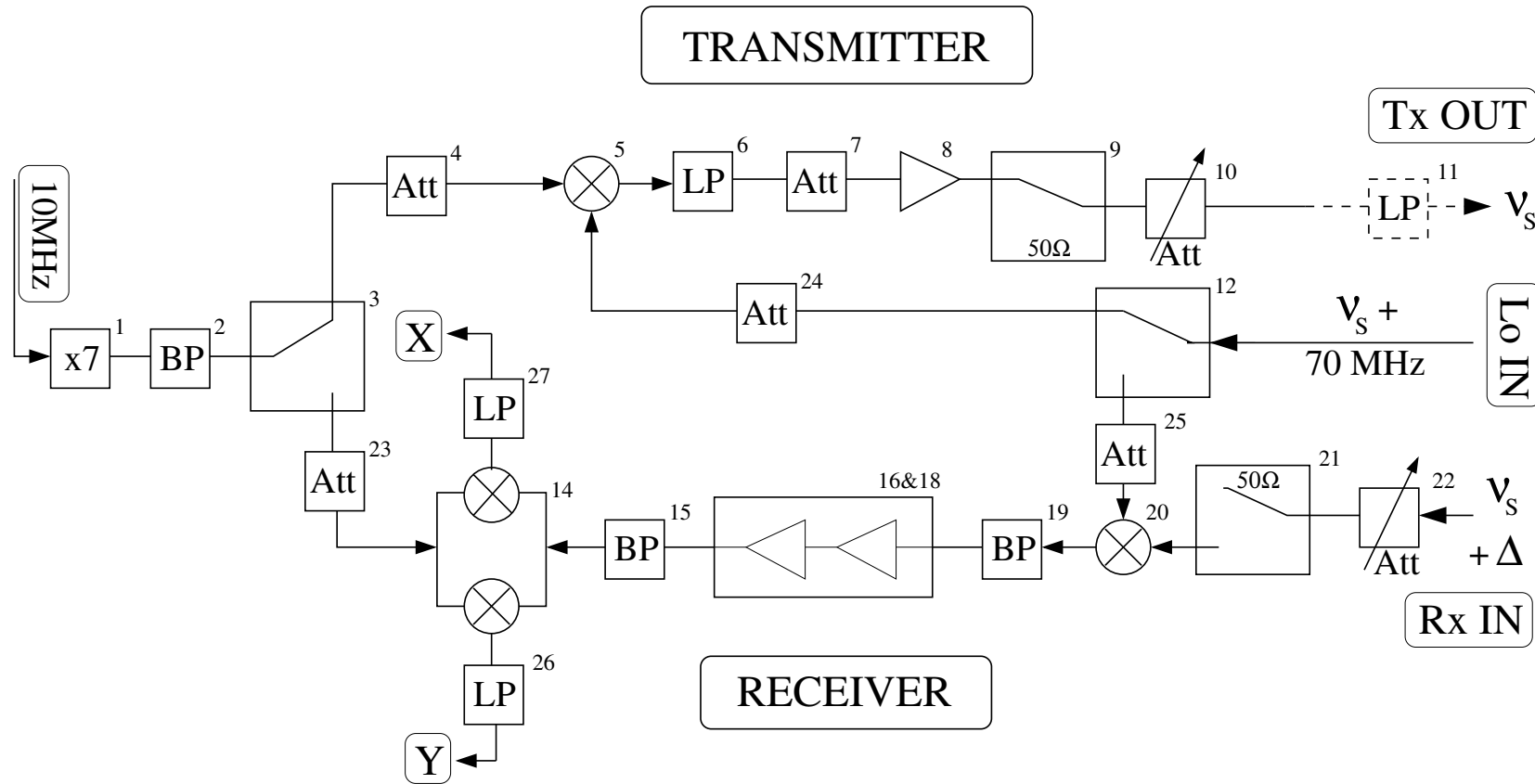
Figure 4.6: Schematical description of the 70 MHz spectrometer. Switches are on transmit mode with logical 0.

The input for the receiver path is *Rx IN*. The signal from the preamplifier has the chosen frequency ν_s with a band width window of $\pm\Delta$. The preamplifier amplifies the spin signal coming from the probe head and can be attenuated *(22)* with up to 45.5 dB. After switch *(21)* this signal is mixed *(20)* with the signal from switch *(12)* to get the spectrometer working frequency range of 70 MHz $\pm \Delta$. The overall band width is reduced by a 70 MHz band pass *(19)* to ± 7 MHz. In the next stage *(16 & 18)* this signal is amplified. After another 70 MHz band pass filter *(15)* the signal enters to the I&Q demodulator *(14)* to be mixed with the 70 MHz frequency from switch *(3)*. The output signals of the spectrometer are $\pm\Delta$, separated in two 90° phase-differing signals X and Y which are connected to channel 1 and 2 of the digital oscilloscope. Both signals pass a low pass filter *(26)* and *(27)* of 1.9 MHz.

4.2.2   Power supply and the TTL control circuit

The power supply is equipped with two *POWER-ONE HA5-1.5/OVP-A* power units delivering 0.125 A for $+5$ V and -5 V each, and one *POWER-ONE HC15-3-A* unit with 0.5 A at $+15$ V[4.7].

For the TTL control signal we equipped a board with a *FAIRCHILD 74AC00* Quad 2-Input NAND Gate IC containing 4 NAND gates, one for each switch of the spectrometer.

As explained before we need a logical `1` for receiving and a logical `0` for transmitting. However, what we get from the pulse generator is a logical `1` for transmitting and a logical `0` for receiving. It has to be pointed out that the main subject of the control circuit is to keep the spectrometer on receive-mode in any case, and switch to transmit-mode just for sending a pulse.

To prevent the spectrometer to switch to the transmit-mode in case of

- a broken or floating connection to the pulse controller, the input line of the control circuit is grounded to pull down the line to a logical `0`,

- a broken or floating connection between control circuit and spectrometer, each TTL line is pulled up to $+5$ V with a 1 kΩ resistor (logical `1`) inside the spectrometer.

[4.7]Time lag fuses are used.

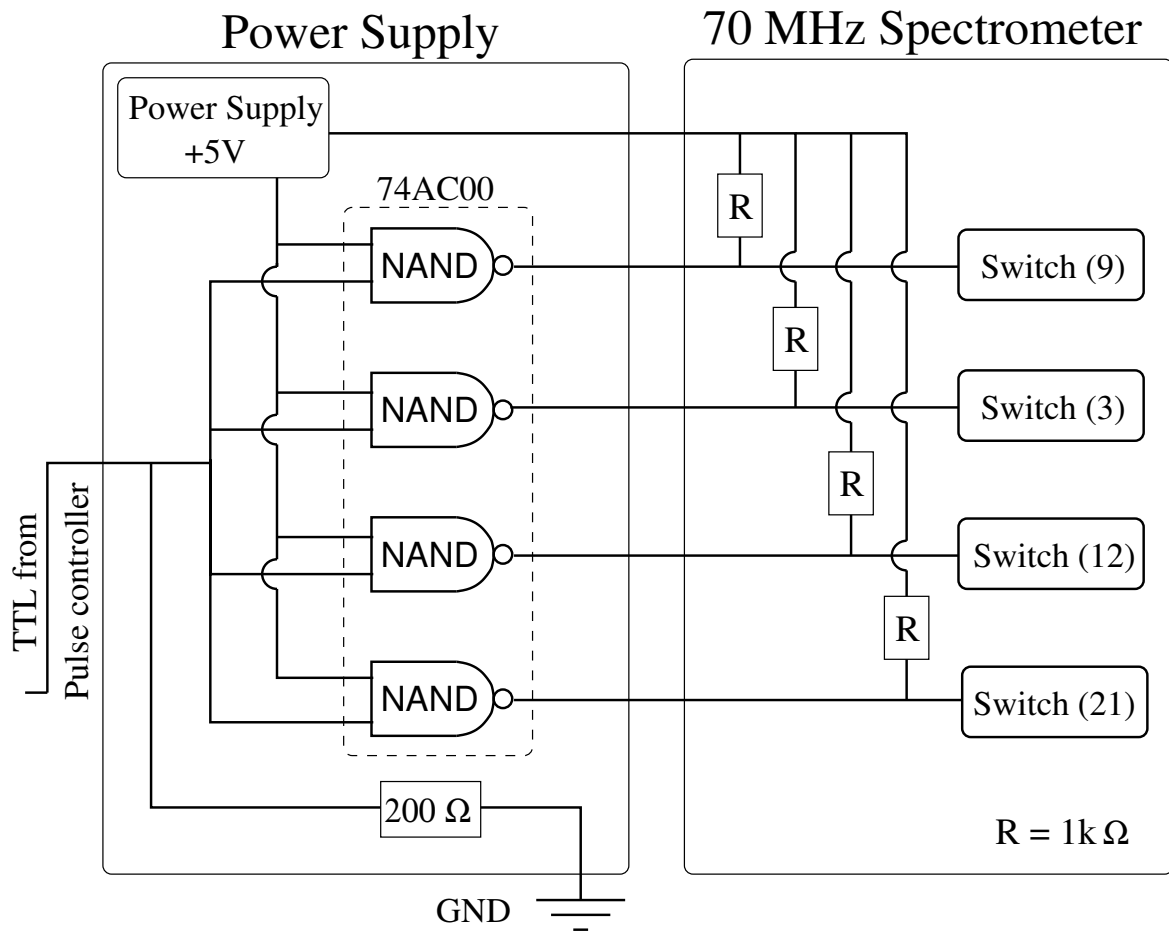## Power Supply   70 MHz Spectrometer

Figure 4.7: TTL control circuit of the switches in the spectrometer

4.2.3 Comments on the construction of the 70 MHz Spectrometer

The construction of the home-made spectrometer contained different stages of handcraft. The hardware part in the mechanical workshop consisted mainly of preparing the front, back, and base plates of both, spectrometer and power supply. The baseplate had to be prepared to hold all the elements. For the spectrometer we made a baseplate out of copper to have a grounded base, both for heat transport and electrical ground. The electrical part, done in the electronics laboratory, consisted of ordering cables, soldering, constructing, and adapting $50\,\Omega$ semi-rigid lines to connect the different RF elements. In view of the high working frequencies of the spectrometer we had to assure that the setup was electrically well insulated and that there were no parasitic leaks.

The connectors lineup between the spectrometer and its power supply, and between pulse controller and power supply, respectively, are listed in the appendix C.

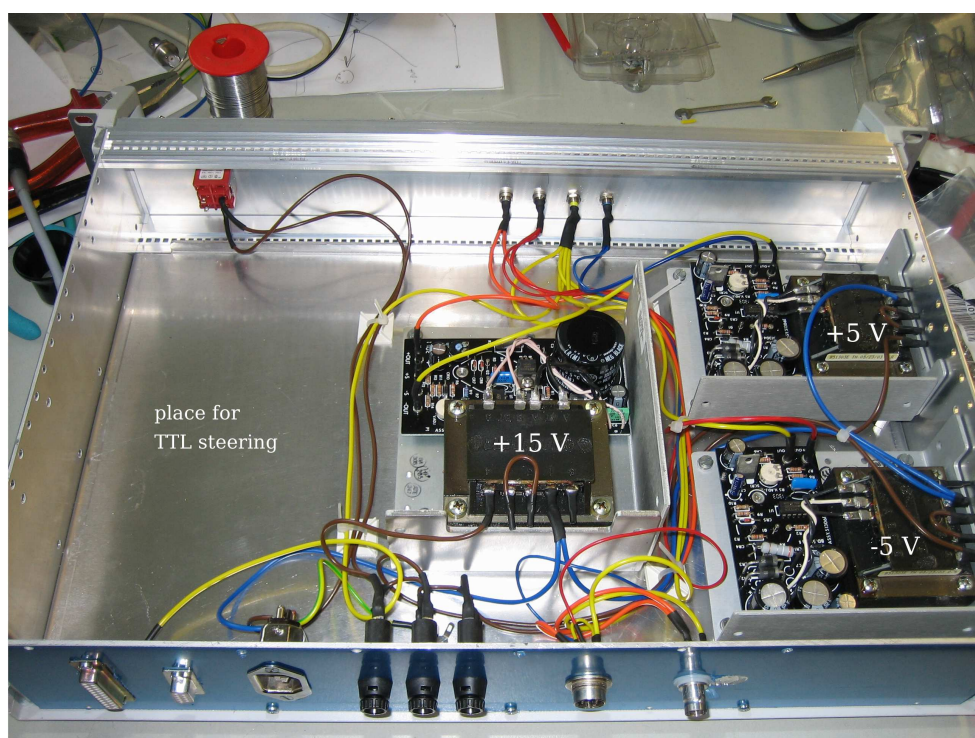In section 5.2 the spectrometer tests will be presented.

Figure 4.8: Top: 70 MHz spectrometer. Bottom: Power supply for the spectrometer.

Chapter 5

Testing Procedure

5.1 NMR probe head and magnetic-field homogeneity of the PPMS

In this section the behavior of the probe head in the PPMS will be discussed. After a first cool down, performance check, the magnetic field homogeneity was analyzed, and drift properties of the PPMS were examined. For this whole testing series we used our home-made 70 MHz spectrometer.

As sample D_2O of 99.9 % purity was used. The Deuterium nucleus was examined, It consists of a proton and a neutron and has spin $I = 1$. The gyromagnetic factor $\bar{\gamma} = \frac{\gamma}{2\pi}$ of Deuterium is 6.5349 MHz/T.[5.1]

5.1.1 Cool down behavior of the probe head

As the probe head was expected to work well at low temperatures, the first check focused on the mechanical behavior, where we wanted to make sure that the tuning and matching of the resonance circuit could still be done without the capacitors getting stuck due to material dilatation or freezing out of gases. At the same time the behavior of the CERNOX thermometer placed next to the sample could be monitored. The probe head was mounted into the PPMS and the resonance circuit was tuned and matched properly. After a night stable at room temperature (300 K) the cooling process started, matching and tuning was frequently checked and adjusted. The capacitors were indeed still movable down to 1.8 K, the final puck temperature. During cool down the CERNOX thermometer at the sample position was tightly following the temperature measured by the PPMS puck thermometer.

Concerning temperature control below 10 K, best stability was obtained by interrupting a cool down from room temperature at 10 K for 30-45 minutes before going lower in temperatures.

[5.1]With equation (2.6)) $\Longrightarrow \nu_L = \bar{\gamma} B_0$.

5.1.2   Magnetic-field homogeneity of the PPMS

For this homogeneity test a spherical glass container, with an outer diameter of $9\,\text{mm}$, was filled with D_2O. One end of the container (closed by melting) had an additional $8\,\text{mm}$ long tail which was also containing a small amount of D_2O. To tune the resonance circuit at the deuterium larmor frequency $\nu_L = 22.915\,\text{MHz}$ at a magnetic field of $3.5\,\text{T}$, a capacitor $C_{M_p} = 220\,\text{pF}$ parallel to the matching capacitor C_M was added, and to broaden the resonance a resistance $R = 5.6\,\Omega$ was placed between the coil and the tuning capacitor C_T.
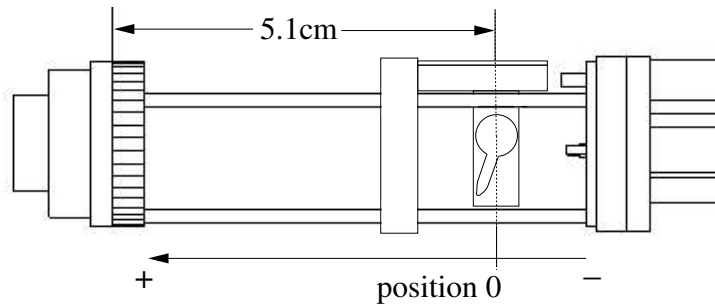

Figure 5.1: Positioning of the spherical glass container with D_2O in the sample-coil holder.

The probe was installed as seen in figure 5.1, with the sphere centered at $5.1\,\text{cm}$ above the puck surface, which corresponds to the center of the magnetic-homogeneity region following the PPMS manual [4]. For the measurement, the signal was optimized to get a 90°-pulse length of $19\,\mu\text{s}$ with a transmitter attenuation of $24\,\text{dB}$ and a 180°-pulse of $39\,\mu\text{s}$. The Fourier transformed signal of the FID is shown in figure 5.2.

The Fourier transformed signal shows a narrow peak on the left side of the main peak and a plateau to the right with approximately 2/3 of the slim peak's intensity. The *full width at half maximum* (FWHM) is about $\Delta_\nu = 1.9\,\text{kHz}$, which corresponds to a magnetic field inhomogeneity of $\Delta_B = 2.7 \times 10^{-4}\,\text{T}$. We obtain $\Delta_B/B = 0.0083\,\%$ which compares reasonably with the $0.01\,\%$ reported in the PPMS specifications for a cylindrical volume of $5.5\,\text{cm}$ height with $1\,\text{cm}$ diameter [4].

To perform a measurement with a smaller, symmetrical probe a smaller test tube was taken and filled with heavy water[5.2], sealed with rubber, inserted into a PVC tube that fitted into the sample-coil holder, and placed with its center axis at the height of $5.1\,\text{cm}$ above the puck surface (see figure 5.3).

With this setup, measurements at magnetic fields of $3.5\,\text{T}$ $(22.916\,\text{MHz})$ and $9\,\text{T}$ $(58.954\,\text{MHz})$ were made for purpose of comparison. The results are shown in the following table.

[5.2]Cylindrical D_2O volume of $3\,\text{mm}$ diameter and $4.7\,\text{mm}$ height.
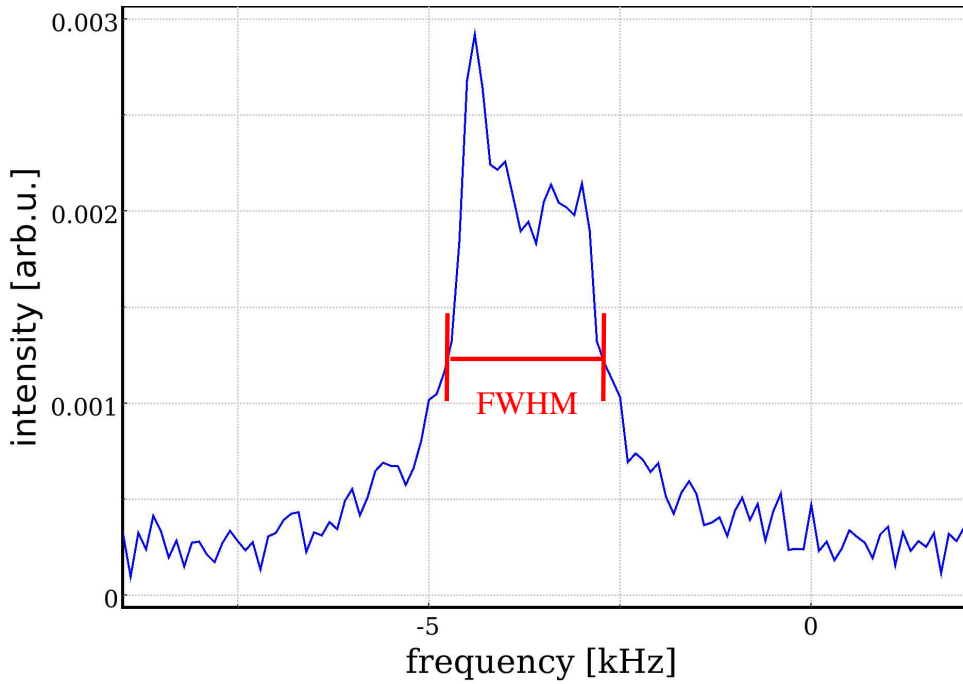
Figure 5.2: Fourier transformed of the deuterium spin signal. The FWHM is about $\Delta_\nu = 1.9\,\text{kHz}$.

$B\,[\text{T}]$	$\Delta_\nu\,[\text{kHz}]$	$\Delta_B\,[10^{-4}\,\text{T}]$	$\Delta_B/B\,[\%]$
3.5	1.2	1.8	0.0052
9	2	3.1	0.0034

To prove that there was no field inhomogeneity produced by the probe head itself, a test probe head was built having a plexiglass tube to guide a coax cable down to the sample space with a resonance circuit containing the same coil-sample holder as before. The signal was similar to the one with our NMR probe head, and no further narrowing of the FWHM could be detected.

Figure 5.3: Positioning of the small D_2O test tube sample in the sample-coil holder.

5.1.3   Position dependent magnetic-field homogeneity

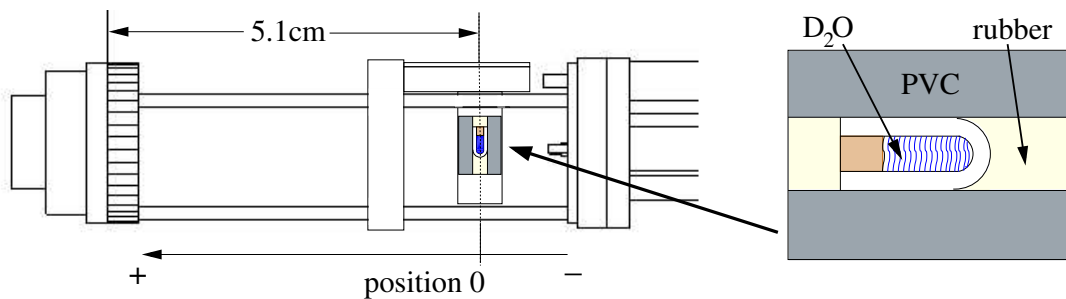To check the position dependence of the magnetic-field homogeneity we used the same sample as shown in figure 5.3. This was done at a field of 3.5 T with a spectrometer frequency of 22.916 MHz and using the same resonance circuit as with the previous 3.5 T measurements.

The sample plateau was attached at different heights for each measurement. Our positioning scale was set as shown in figure 5.3, where position 0 corresponds to the center of magnetic homogeneity region at 5.1 cm above the puck surface [4]. At this position several measurements were taken with and without Berilco screws holding the sample plateau, yielding almost identical results.

The result of FWHM Δ_ν vs. position is presented in figure 5.4.
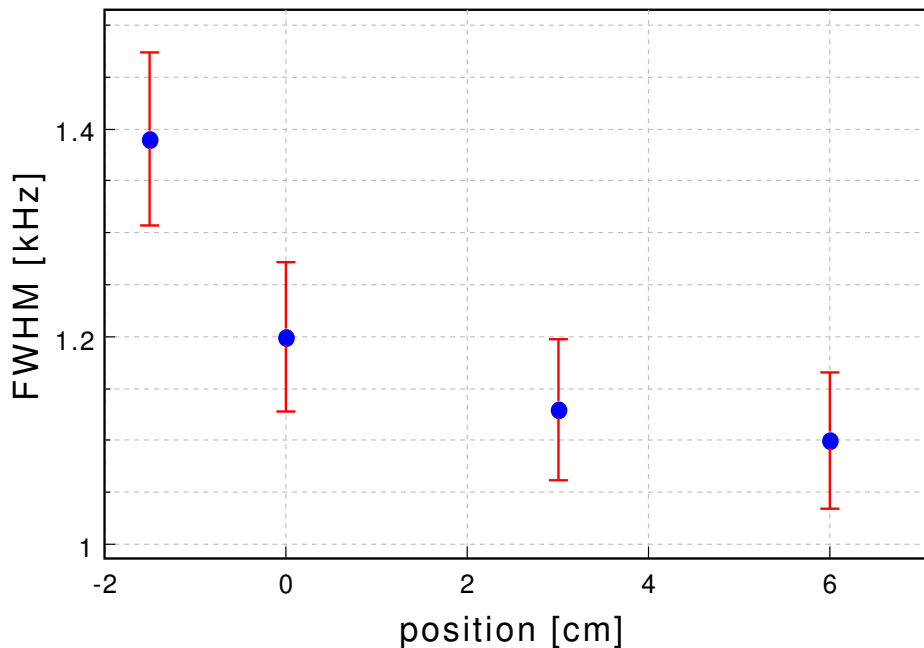

Figure 5.4: Position dependent field spread.

We noticed a decrease of the FWHM when moving the sample down towards the puck. The FWHM-measurement at +6 cm is about 10 % narrower than the one at 0 cm. This could indicate a slight magnetic inhomogeneity produced by the probe head around the position of the tuning and matching capacitor.

5.1.4   Drift of the magnetic field

The drift of the magnetic field of the PPMS was tested in two ways. The first test was to check fluctuations of the magnetic field on a short time scale. For this purpose, echos were produced with different pulse spacing times τ during which the echos stability was observed. No fluctuations were detected. With a spacing time of about 70 ms the echo started to become smaller, to finally disappear at a spacing time of 100 ms. This can be explained with the diffusion of the molecules in the D_2O liquid.

The second measurement was made to observe a drift over a larger time scale and to see the difference in drifting between using the linear-approach mode or the oscillating-approach mode in setting the field (section 3.3). Both of the measurements were done with a magnetic field of 3.5 T at a spectrometer frequency of 22.921 MHz, a 90°-pulse of 15 μs, a transmitter attenuation of 22 dB, and with the resonance-circuit setup as used before. The resulting data is shown in figure 5.5.
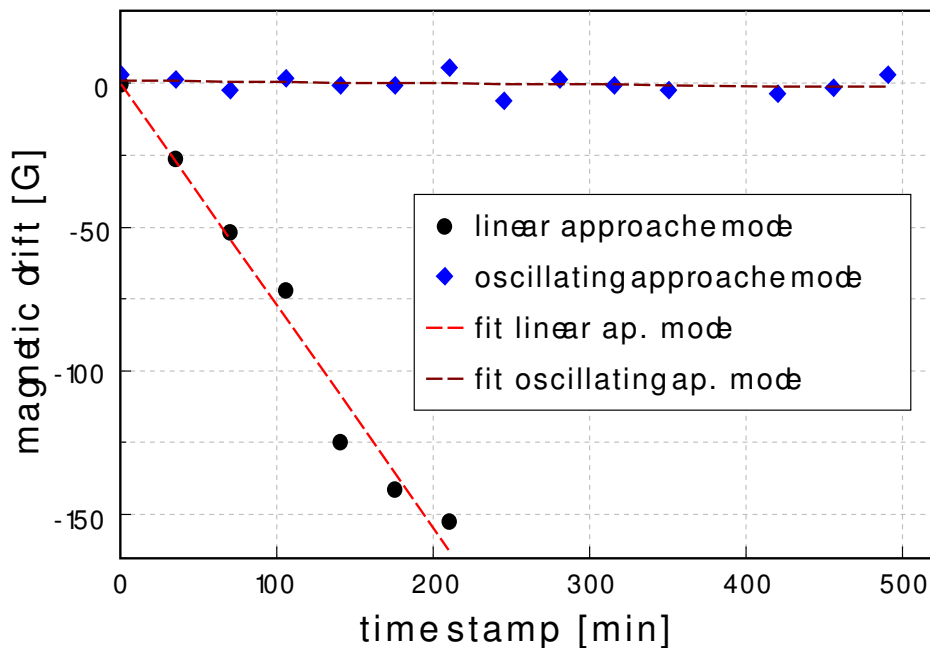
Figure 5.5: Magnetic drift of the PPMS. With the linear-approach mode the magnetic field drifts at a rate of -46.49 G/h, while whith the oscillating approach the drift rate is -0.26 G/h.

We measured a fast drift using the linear-approach mode, and no clearly detectable drift with the oscillating-approach mode. Making a linear-fit for both approaching modes, we obtain -0.26 G/h for the oscillating approach and -46.49 G/h for the linear approach. By observing the resulting FWHM of the resonance lines of these measurements, we can

also observe a difference between the two approaching modes. For the linear mode we get a mean value $\Delta_\nu = 1.20\,\text{kHz}$ ($\Delta_B = 1.84 \times 10^{-4}\,\text{T}$), as compared to a value $1.07\,\text{kHz}$ ($1.64 \times 10^{-4}\,\text{T}$)in the oscillating mode indicating that the oscillating-approach mode produces a slightly more homogeneous field.

5.1.5   Summary

The NMR probe head has shown good performance, handling and stability in high magnetic fields and also at low temperatures. The magnetic-field homogeneity is in the range of $0.01\,\%$ as specified by Quantum Design [4]. The measurements of the position dependent magnetic field homogeneity show a slightly better homogeneity below the specified center of magnetic-homogeneity region. The faster linear approach mode shows a clear drift of the magnetic field while the more time consuming oscillating-approach mode results in a stable magnetic field with a very small drift and a slightly better homogeneity.

5.2   70 MHz spectrometer

In the 70 MHz spectrometer tests, an overload problem was discovered in the receiver path, which is described in the next subsection 5.2.1.

A signal-to-noise ratio comparison of the 70 MHz spectrometer with the Lupotto II spectrometer running with 95 MHz was also made (see subsection 5.2.2). For a description of the Lupotto II spectrometer, which is an analogue to the Lupotto IV spectrometer, we refer to section 3.2.1 .

To test the spectrometer we made *nuclear quadrupole resonance* (NQR)[5.3] measurements on the Cl^{35} isotope in natrium-chlorate $NaClO_3$ powder, diluted in paraffin oil, a method to prevent any piezo-effect related response of the powder-grains. The natural abundance of Cl^{35} is of 75.78%, and it has a nuclear spin $I = 3/2$.

5.2.1   Overload of the spectrometer

By using the MITEQ AU-1448 broadband preamplifier with a gain of 53 dB we discovered that after the pulse, the receiver path of the spectrometer was not working well for a short time due to an overload caused by extrusion of the transmitting pulse. As an FID was clearly seen, the possibility an electrical sparking in the resonance circuit could be excluded. By changing the preamplifier to a MITEQ AU-1313 with a gain of about 43 db this paralyzing of the spectrometer could be eliminated. For a safe operation of the spectrometer a standard receiver attenuation of 8 dB was chosen, with which no sign of overload could be seen. In figure 5.6 the overload lasting for $\approx 23\,\mu$s after a 180°-pulse is shown.

5.2.2   Comparison: 70 Mhz spectrometer vs. Lupotto II

To make a signal-to-noise ratio comparison of the spectrometers we optimized the 70 MHz spectrometer for a 90°-pulse at resonance (frequency of 29.931 MHz). Then, the amplitude of the FID and its noise was measured at the slightly off resonance frequencies of 29.934 MHz and 29.937 MHz. The same procedure was applied with the Lupotto II spectrometer. Because of the strong temperature dependence of the NQR frequency of the Cl^{35} nuclei in $NaClO_3$, the repetition time between two pulses was extended to 2 s. For each measurement we used 50 sweeps.

[5.3]A technique that will not be described any further. It was used for hardware testing only and has no relevance for the present work.
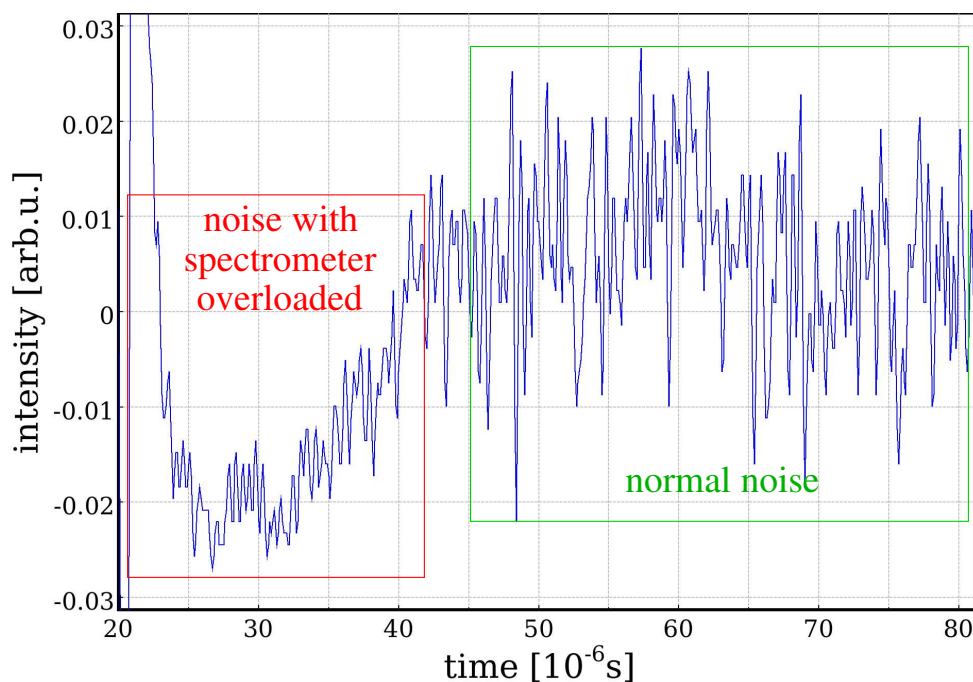
Figure 5.6: Spectrometer overload. The noise shrinks to about a third of the normal noise level for $\approx 23\,\mu$s. The measurement was done with a 180°-pulse, and no attenuation and the MITEQ AU-1448 broadband preamplifier.

The signal-to-noise ratio was calculated by taking the real part of the *root mean square* (RMS) of the respective signal as shown in the following formula:

$$\text{ratio} = \frac{\Re(\text{RMS(signal)})}{\Re(\text{RMS(noise)})} \ . \tag{5.1}$$

The ratios that where calculated from the FID are:

frequency	70 MHz spectrometer	Lupotto II spectrometer
29.934 kHz	7.3552	6.0938
29.937 kHz	7.3704	6.2433

The signal-to-noise ratio of the 70 MHz spectrometer is comparable (slightly better) to the one of the Lupotto II spectrometer, although it must be pointed out that the Lupotto II spectrometer was adapted to have an equal FID amplitude of about 200 mV peak-to-peak as on the 70 MHz spectrometer. To do this the amplification of the Lupotto II spectrometer had to be decreased to a minimum, with a negative influence on its signal-to-noise ratio.

5.2.3   Summary

The 70 MHz spectrometer has shown a good performance. Nevertheless we have noticed several disadvantages, e.g., the overload problem that could be relevant for measurements of materials with a fast FID.

We have also to conclude that the spectrometer amplification is too weak, but this situation could be improved by using an additional amplifier (Mini Circuits/ZFL-500) after the dual amplifier (Wenzel Associates/LNFDA-70-(-46)-(-10)), see section 4.2.1 and appendix C.2) in the receiver path.

Another limitation of the spectrometer is that it has no phase-modulation possibilities as the 4-phase modulators in the Lupotto series that is used in the `t2seq14`, a Matlab function described in section 3.2, to clean the echos. However, this limitation can be eliminated by using a fast phase switchable frequency generator.

Chapter 6

LaBaNiO$_{4-\delta}$ Investigation

LaBaNiO$_{4-\delta}$ is considered to be a promising candidate to represent a "parent compound" of Ni-based superconductors. It is believed that, like it is the case in La$_2$CuO$_4$, spin $I = 1/2$ antiferromagnetism and Mott-Hubbard insulation are important ingredients for the occurrence of superconductivity on subsequent doping of the compound with charge carriers [9].

The main questions to solve for this project are:

 a) Is LaBaNiO$_4$ really an insulator at $T = 0\,$K?

 b) Is Ni in a low-spin $s = 1/2$ state, and if so, has it an anti-ferromagnetic ordering at a finite temperature?

The contribution of this diploma thesis to these LaBaNiO$_{4-\delta}$ investigations was to perform a NMR-study on this compound. Previous investigations done on this polycrystalline compound are rare. As a starting guideline for this research we used the results of Refs. [9], [10] and [11].

6.1 Sample characterization

The compound LaBaNiO$_{4-\delta}$ is a structural analogue to the compounds La$_2$NiO$_4$, LaSrNiO$_4$ and the well known cuprate La$_2$CuO$_4$ ([11],[10] and [12]). Stoichiometric LaBaNiO$_{4-\delta}$ belongs to the tetragonal space group I4/mmm (No. 139) with cell parameters $a = 3.8693$ Åand $c = 12.8803$ Å. Its structure and the X-ray Guinier spectra are shown in figure 6.1.

LaBaNiO$_{4-\delta}$ has a molar weight of 399.0085 g/mol. It has been reported that LaBaNiO$_{4-\delta}$ is semiconducting [10] and it has been claimed that it shows a crossover form a high-spin to a low-spin Ni state upon cooling down below a temperature of 100 K.
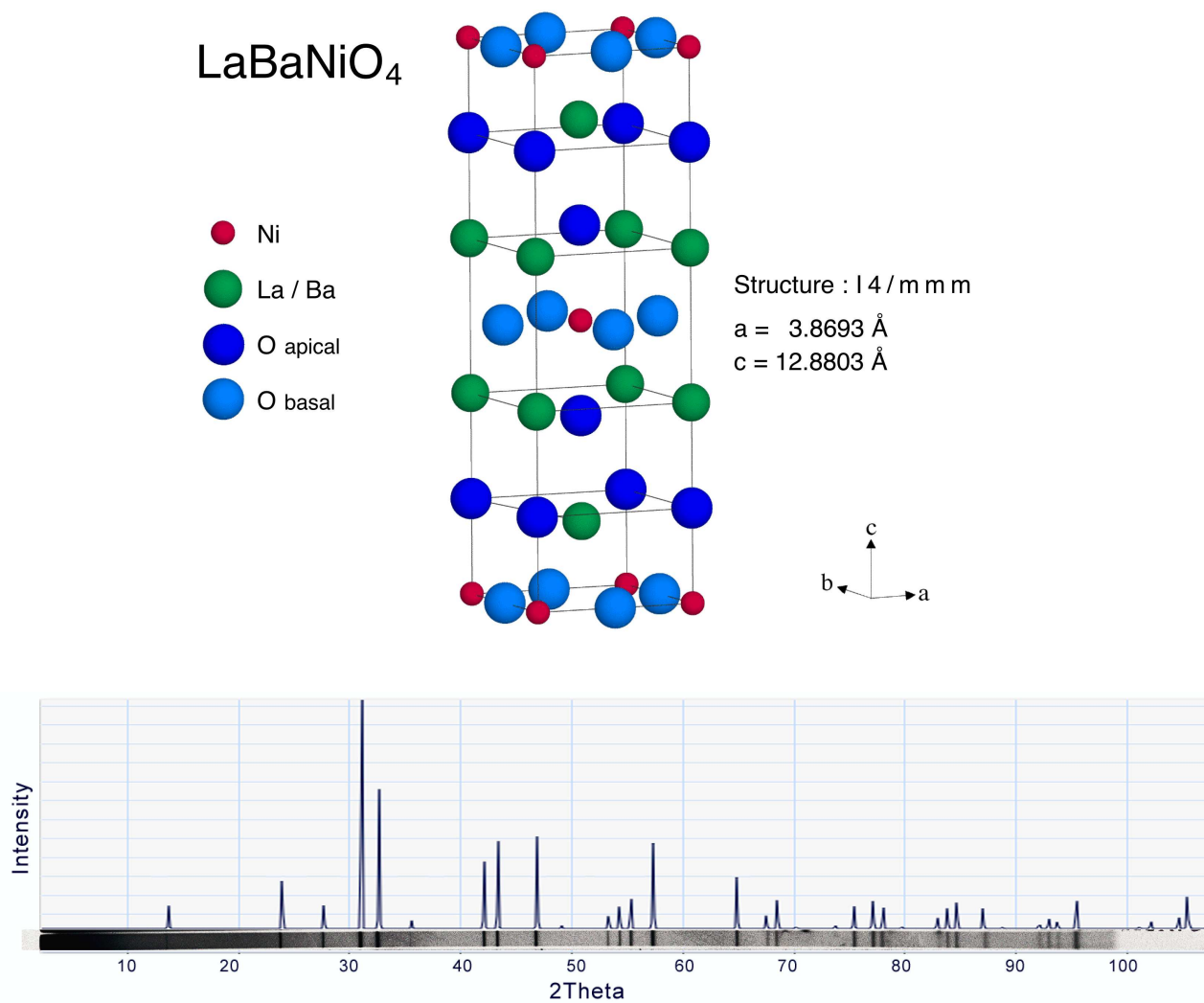
Figure 6.1: Top: I4/mmm structure of LaBaNiO$_4$. In between two basal NiO planes are two apical La/BaO layers. Bottom: Calculated X-ray Guinier spectra, in agreement with the X-ray film pattern. The presence of impurities above 5 % sample volume can be excluded.

The nuclear data relevant for NMR are listed in table 6.1.

nucleus	spin	nat. abundance [%]	$\bar{\gamma}\,[\mathrm{T}^{-1}\mathrm{s}^{-1}]$
^{139}La	7/2	99.91	6.0036
^{137}Ba	3/2	11.32	4.7314
^{135}Ba	3/2	6.59	4.2294

Table 6.1: Relevant nuclear data for NMR research on LaBaNiO$_{4-\delta}$

The preparation of the polycrystalline sample was done through a standard wet chemical procedure. In a solution of distilled water (50 ml) and nitric acid NHO (10 ml) the corresponding metal nitrates, La(NiO$_3$)$_3$, Ba(NiO$_3$)$_2$, and Ni(NiO$_3$)$_2$ were mixed. The liquid was then warmed up and evaporated. The remaining powder of nitrates was ground in a mortar and pre-reacted at 900° C for 24 hours in air. The color of the powder has turned from light green to black at this stage.

This powder is ground in a mortar again, pressed into a pellet, and sintered at 1100° C for 3 days in air. The X-ray diffraction done with a Guinier camera (Cu K$_{\alpha 1}$ radiation) showed no impurities above 5 % sample volume (see figure 6.1). At the same time the I4/mmm structure was confirmed.

Neutron diffraction experiments, chemical analysis, electrical resistivity, magnetic susceptibility, and specific-heat measurements were done on the sample and are presented in Ref. [9]. The chemical analysis showed an oxygen deficiency of $\delta = 0.15(1)$.

A Torlon capsule was filled with LaBaNiO$_{4-\delta}$ powder. The cylindrical volume of the powder sample was 4 mm in diameter at 1.5 cm length, with 845(5) mg of sample mass.

6.2   Summary of NMR experiments

This section is a resume of the experimental part on LaBaNiO$_{4-\delta}$. A short discussion for
each measurement is given, while the general discussion combining these measurements is
presented in the next section.

Because of better amplification and phase modulation possibilities, the Lupotto IV spec-
trometer was chosen for these NMR experiments. The spin-echo method, described in the
theory section 2.3.1, was used.

To get a value for the intensity of the spin response at a given magnetic field value, the
absolute value of the integral over the echo was calculated. For this purpose, the `fldscan1`
Matlab function script described in section 3.4 was used. The used parameters are col-
lected in tables, listing coil setup C #, 90°-pulse duration $t_{p_{90}}$, 180°-pulse duration $t_{p_{180}}$,
repetition time t_{rep}, the spacing time between the pulses τ, transmitter attenuation Att$_T$,
the receiver attenuation Att$_R$, amount of sweeps sw #, set temperature T, magnetic field
value B, and the chosen spectrometer frequency ν_s.

6.2.1 ^{139}La frequency scan at 8.5 T

The calibration of the pulse lenghts of ^{139}La was done with a powder of the metallic cubic
compound LaB$_6$. To prevent electrical conduction between the powder grains, paraffin
oil was added and mixed with the powder. Apart form the pulse lengths, the parameters
were the same as for the subsequent ^{139}La measurement in LaBaNiO$_{4-\delta}$. The optimized
reference pulses were $t_{p_{90}} = 7.5\,\mu$s and $t_{p_{180}} = 15\,\mu$s. The FWHM Δ_ν of the measured ^{139}La
resonance peak in LaB$_6$ was 16.7 kHz.

To have an overview at the ^{139}La spin spectrum in LaBaNiO$_{4-\delta}$, a frequency scan was
done manually at a magnetic field of 8.5 T[6.1].
The following parameters where used:

B [T]	T [K]	$t_{p_{90}}$ [μs]	$t_{p_{180}}$ [μs]	t_{rep} [ms]	τ [μs]	Att$_T$ [dB]	Att$_R$ [dB]	sw #	C #
8.5	300	2	3.5	100	400	9	22	500	4

Discussion: The thus obtained data are plotted in figure 6.2. One can see a sharp peak
with its maximum at 51.25 MHz, together with a broad, smaller peak. To distinguish this
two peaks we will define the narrow peak as peak A and the broad peak as peak B (see
figure 6.2, upper left panel).

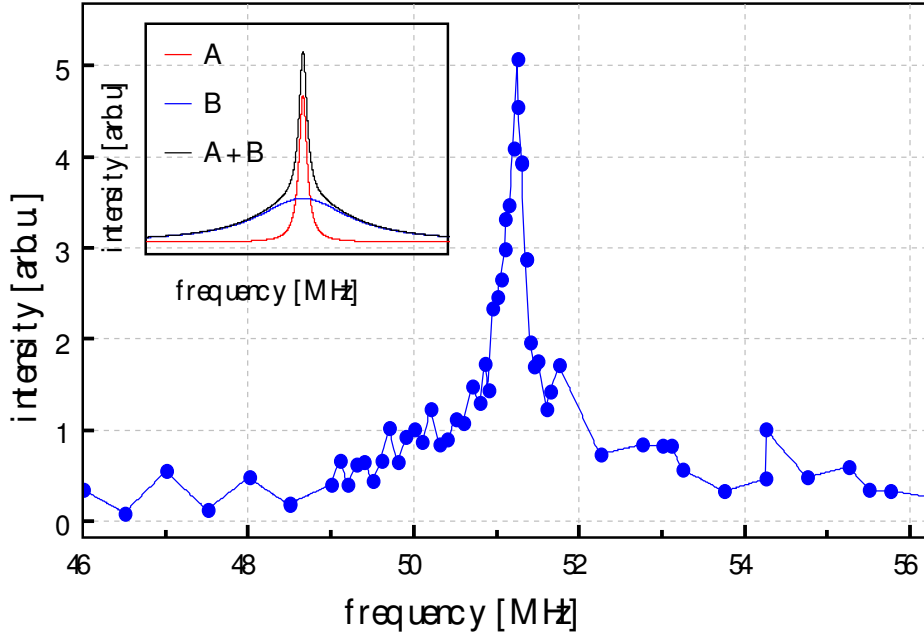[6.1]The resonance circuit was matched for each frequency.

Figure 6.2: Room temperature ^{139}La frequency scan at $B = 8.5\,\mathrm{T}$. A narrow distinct peak A can be seen with an underlying flat peak B. Upper left panel: Fit function (6.1) for Peaks A, B, and A + B.

Following the theory of first-order quadrupole interaction in section 2.4.1 6 satellites and a central line (peak A) are expected (see figure 2.3 on page 11). There are no clear satellites visible in the data. Imperfections in the crystal grains (presumably related to the oxygen deficiency in the structure) may be responsible for a strong broadening of the satellites, producing one broad line like peak B (section 2.4). The possibility that peak A also contains some satellites can not be excluded.

The line widths were calculated by fitting the data points with the sum of two Lorentz functions using the Levenberg-Marquardt algorithm,

$$f(\nu) = y_0 + \underbrace{A\frac{2}{\pi}\frac{\Delta_A}{(4(\nu - \nu_p)^2 + \Delta_A^2)}}_{\text{peak A}} + \underbrace{B\frac{2}{\pi}\frac{\Delta_B}{(4(\nu - \nu_p)^2 + \Delta_B^2)}}_{\text{peak B}} \; . \qquad (6.1)$$

y_0 is the intensity offset, ν_p is the frequency at peak maxima, $2A/\pi$ and $2B/\pi$ the respective peak amplitudes, Δ_A and Δ_B the respective FWHM. The results are presented later in table 6.2 in the discussion section 6.3.

We note that a spin echo response was still detectable at the limiting frequencies of this measurement, 44.0 MHz and 57.2MHz (not shown in figure 6.2).

6.2.2 ^{139}La field scan at 51.2 MHz

Three field scans at the temperatures 300 K, 40 K, and 4 K where done starting form 9 T and decreasing magnetic field. To get the peak maxima at 8.5 T we chose $\nu_s = 51.20157$ MHz. Three different field intervals were measured at room temperature $T = 300$ K and combined afterwards. Scans from 9 T to 8.7 T and form 8.3 T to 6 T were done in 0.02 T steps, and from 8.7 T to 8.3 T in 0.01 T steps[6.2]. At $T = 40$ K and $T = 4$ K field scans were made from 9 T to 7 T and 9 T to 7.7 T respectively, both with 0.02 T steps.
The used parameters are listed below.

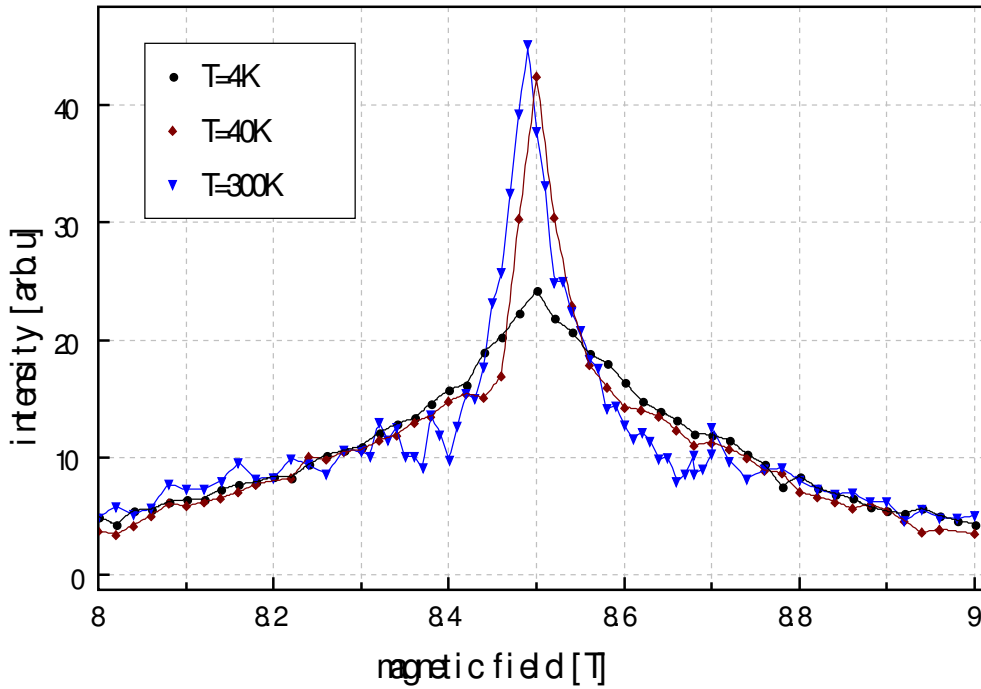| T [K]	ν_s [MHz]	$t_{p_{90}}$ [μs]	$t_{p_{180}}$ [μs]	t_{rep} [ms]	τ [μs]	Att$_T$ [dB]	Att$_R$ [dB]	sw #	C #
300	51.20157	2	3.5	50	20	9	22	1000	4
40	51.20157	2	3.5	50	30	9	22	1000	4
4	51.20157	2	3.5	2000	30	9	37	28	4

Figure 6.3: ^{139}La field scans from 9 T to 8 T ($\nu_s = 51.2$ MHz).

[6.2]For the 8.7 T to 8.3 T measurement sw# = 300 was used instead of 1000.

Discussion: All three field scans are shown together in figure 6.3. The figure focuses on the peaks. The tales of the flat peak B and the noise field range below 8 T is not shown. In the figure, the scans from the three temperatures are scaled to match each other using the integrated intensities of the spectra from 8 to 9 T.

If we compare with the frequency-scan data, we observe the large narrow peak A and the broad small peak B in the measurements at 300 K and 40 K. In the measurement at 4 K, peak A appears to be broadened and its intensity is decreased, while the shape of peak B seems to be unaffected.

Comparing the spectra at 4 K and 40 K, a slight shift of the room temperature peak A to lower magnetic fields can be observed. In addition, a downward structure at the transition from peak A to peak B, on both sides of peak A at $T = 300$ K, could indicate satellites.

The Δ's of the three measurements, calculated with the same fit function (6.1) as before, are listed in table 6.2 in section 6.3. The calculated Δ data show a slight increase from 300 K to 40 K, and a doubling of the width from 40 K to 4 K for peak A. The width of peak B seems to slightly increase with temperature.

6.2.3 ^{139}La field scan at 30.2 MHz

For comparison, field scans at 30.20015 MHz where made at the same three temperatures 300 K, 40 K, and 4 K. At 4 K and 40 K the field scans were made starting from 6 T down to 4 T with steps of 0.02 T. At 300 K two field scans were made and combined, one from 5.13 T to 4.83 T, and another one from 6 T to 4.7 T, both with 0.02 T steps.
The parameters of the three measurements are listed in the following table:

T [K]	ν_s [MHz]	$t_{p_{90}}$ [μs]	$t_{p_{180}}$ [μs]	t_{rep} [ms]	τ [μs]	Att_T [dB]	Att_R [dB]	sw #	C #
300	30.20015	2	3.5	50	30	9	17	10000	1
40	30.20015	2	3.5	50	30	9	20	50000	1
4	30.20015	2	3.5	1000	30	9	33	400	1

Discussion The corresponding data are presented in figure 6.4. Again, to scale the data plots, the integrated intensities were calculated between 4.7 T to 6 T. A temperature behavior analogous to the ^{139}La measurement at 51.2 MHz can be observed. Peak A has a similar amplitude and width above at 300 K and 40 K. At 4 K we see again the broadening and the decrease in amplitude of the peak.

The peak width summary in table 6.2 shows a slight decrease of Δ for peak A from 300 K to 40 K and again a doubling of the width from 40 K down to 4 K. Peak B shows a width increase with temperature, although less than in the measurement at 51.2 MHz. A slight shift of peak A at room temperature is also visible.
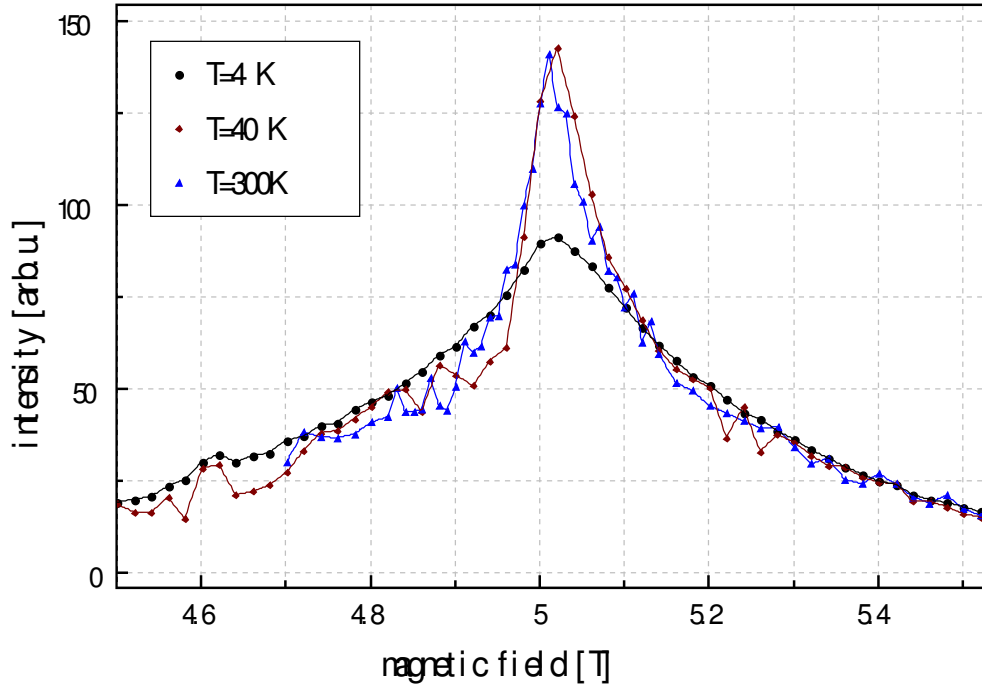
Figure 6.4: ^{139}La field scans from 4 T to 6 T ($\nu_s = 30.2$ MHz).

6.2.4 ^{137}Ba field scan at 40.2 MHz and 40 K

To study the barium nuclei a calibration measurement was performed with BaCl$_2$. The low natural abundance of barium isotopes ^{137}Ba (11.32 %) and ^{135}Ba (6.59 %) made the search for a spin signal very difficult. At a field of 8.5 T and a frequency of 40.308 MHz a ^{137}Ba spin response was found. The echo optimization gave a 90°-pulse length of 8.5 μs and a 180°-pulse length of 17 μs having a transmitter attenuation of 9 dB.

A field scan from 9 T to 7 T with 0.02 T steps was done at a temperature of 40K. The set parameters are given in the following table.

ν_s [MHz]	T [K]	$t_{p_{90}}$ [μs]	$t_{p_{180}}$ [μs]	t_{rep} [ms]	τ [μs]	Att$_T$ [dB]	Att$_R$ [dB]	sw #	C #
40.2081	40	4	8	50	30	9	18	10000	3

Discussion   The measured data are presented in figure 6.5. As it can be seen, the signal-to-noise ratio is low, making the interpretation of the data very difficult. The FWHM $\Delta_B = 0.5(1)$ T ($\Delta_\nu = 2.3(5)$ MHz) of the peak was evaluated from the graph. The increasing intensity for field values below 8 T stems form the high-field tail at the ^{139}La spin signal.
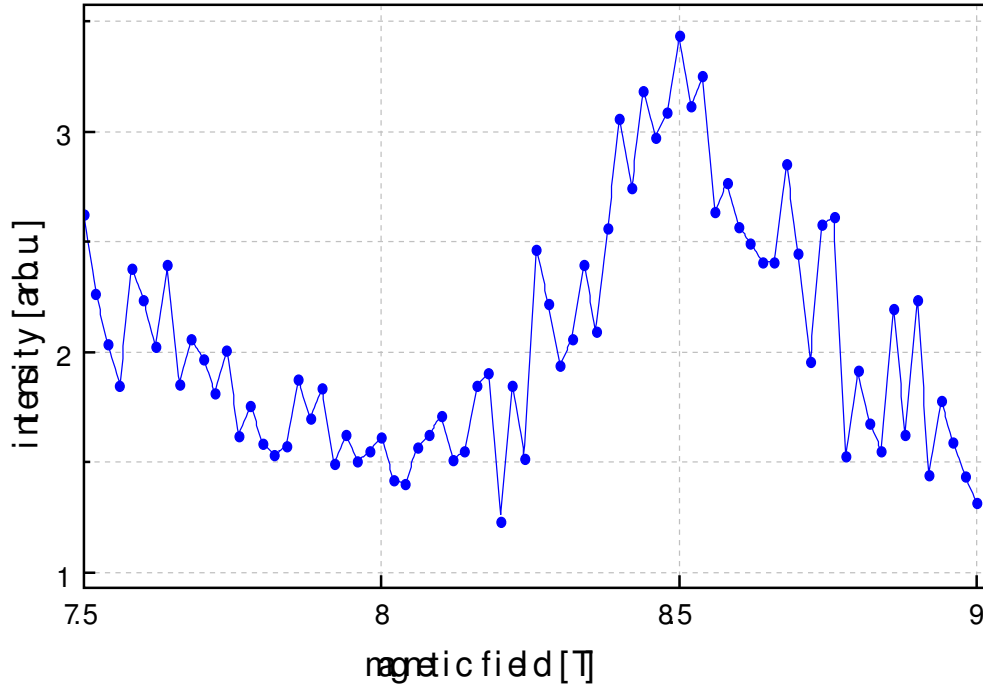
Figure 6.5: ^{137}Ba field scan from 9 T down to 7 T ($\nu_s = 40.2$ MHz) at 40 K.

6.2.5 ^{135}Ba field scan at 33.8 MHz and 40 K

The field scan for ^{135}Ba was performed at a frequency of 33.8 MHz and a temperature of 40 K. The field was scanned from 8.7 T to 7.3 T in 0.1 T steps with the following parameters:

ν_s [MHz]	T [K]	$t_{p_{90}}$ [μs]	$t_{p_{180}}$ [μs]	t_{rep} [ms]	τ [μs]	Att$_T$ [dB]	Att$_R$ [dB]	sw #	C #
33.8352	40	4	8	50	30	9	11	40000	2

Discussion The data are shown in figure 6.6. The graphically evaluated FWHM at the peak is $\Delta_B = 0.55(15)$ T ($\Delta_\nu = 2.3(7)$ MHz). As with to the ^{137}Ba scan, an interpretation of the data is difficult although the peak at 8 T is clearly visible. In order to improve the signal-to-noise ratio, longer signal averaging at each data point would be needed, implicating time consuming scans of up to one week.
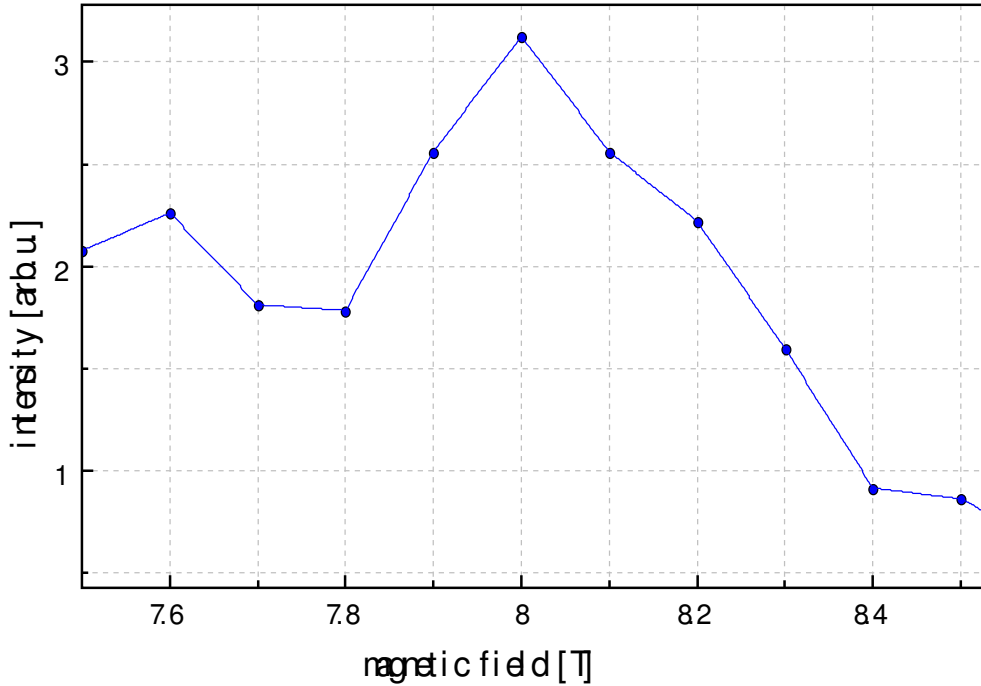
Figure 6.6: ^{135}Ba field scan from 8.7 T to 7.3 T ($\nu_s = 33.8$ MHz) at 40 K.

6.2.6 ^{139}La temperature run at 51.2 MHz

As we have seen in the above ^{139}La measurements above, peak A loses intensity and broadens by cooling down the sample. To analyze this behavior, a temperature run was done manually from 300 K down to 2 K. At each temperature, a 3 point field scan was done with measurements at 8.575 T, 8.5 T, and 8.425 T. This three field values represent the maximum of peak A and the crossover points between peak A and B at each side of peak A, respectively. We will define this points as A_C (8.5 T) for the maximum of peak A, AB_L (8.425 T) for the left crossover, and AB_R (8.575 T) for the right crossover (see upper right panel of figure 6.7).

To prevent electrical breakthrough in the resonance circuit and spectrometer overload at the lowest temperature, the attenuation and pulse times were set accordingly.
The following parameters were used:

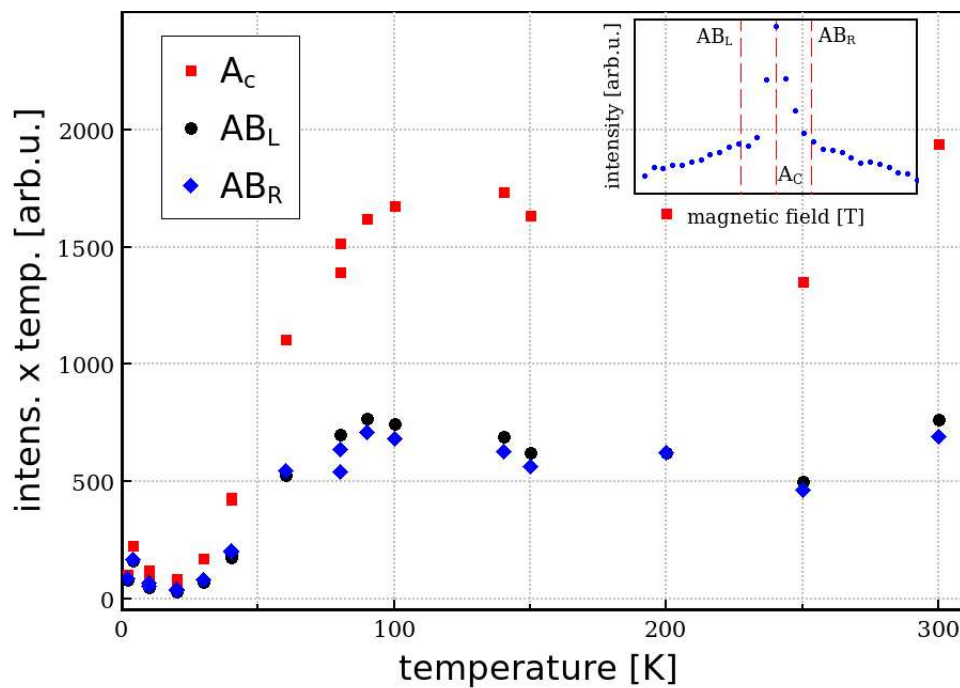| ν_s [MHz]	$t_{p_{90}}$ [μs]	$t_{p_{180}}$ [μs]	t_{rep} [ms]	τ [μs]	Att$_T$ [dB]	Att$_R$ [dB]	sw #	C #
51.20157	1.9	3.7	100	30	9	38	1000	4

Figure 6.7: ^{139}La temperature scan at 51.2 MHz. Upper right panel: Measurement at 30.2 MHz and 40 K to demonstrate the field positions of A_C (8.5 T), AB_L (8.425 T), and AB_R (8.575 T).
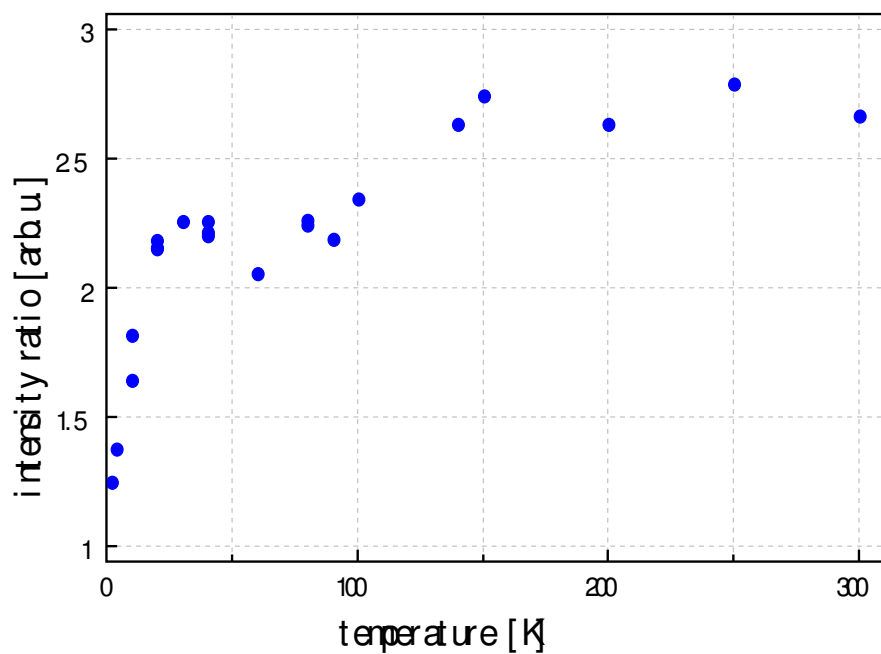

Figure 6.8: Temperature dependent intensity ratio of ^{139}La.

Discussion   In figure 6.7, the product of the measured intensities and the temperature
($I{\cdot}T$) is plotted vs. temperature for all three field values. Following the temperature de-
pendent Boltzmann distribution of the spins [6.3] (see sections 2.1 and 2.2) we would expect
$I{\cdot}T$ to remain constant as a function of temperature. however, we see a decrease of $I{\cdot}T$
below 80 K having a minimum at 20 K. Below 20 K $I{\cdot}T$ has again an increasing tendency.

In figure 6.8 the ratio between A_C and the mean value of AB_L and AB_R is shown as a
function of temperature. We can see a approximately flat ratio between 300 K and 140 K,
an approximately 20 % lower ratio between 100 K and 20 K, and a fast decrease below 20 K.

[6.3]$\propto 1/T$.

6.3 Discussion

Following the descriptions in the theory section 2.4.1 (figure 2.3) we expect 6 satellites for a spin $I = 7/2$ nuclei like ^{139}La. As there are no clear satellites detectable, the calculation of the quadrupole frequency ν_Q from first-order quadrupole effects is difficult.

By taking the field scan at 300 K and 9 T (figure 6.3), assuming that the satellites are located symmetrically around the central peak, and examining the different possibilities of satellite pairs outside of the crossover points between peak A and B, we get a possible range for ν_Q between 0.8 MHz and 4.5 MHz as a first guideline.

A more promising approach is to observe the second-order quadrupole effects (theory section 2.4.2) on the central peak A as a function of the magnetic field. There is an inverse proportionality between the split central line's maxima $\Delta\nu$ and the Larmor frequency ν_L (2.32), while ν_L is proportional to the magnetic field B_0 (2.6). Equation (2.32) can therefore be rewritten as

$$\Delta\nu = \frac{25}{144}\frac{\nu_Q^2}{\bar{\gamma}B_0}[I(I+1) - 3/4] \quad \propto \quad \frac{1}{B_0} \ . \tag{6.2}$$

Because no splitting can be seen (compare to figure 2.4) we set the measured FWHM values $\Delta_{A_\nu} = \Delta\nu$.
The proportionality to the inverse field can be checked by comparing the Δ_A's at each temperature of the 51.2 MHz field scan measurements with the corresponding 30.2 MHz data (table 6.2). For peak B this inverse field dependency is less clear.
We calculate the quadrupole frequency

$$\nu_Q = \sqrt{\frac{144}{25}\frac{\bar{\gamma}B_0 \cdot \Delta_{A_\nu}}{[I(I+1) - 3/4]}} \ . \tag{6.3}$$

The results of ν_Q for the field and frequency scans are also listed in table 6.2.

By comparing the ν_Q's of the frequency scan ($T = 300$ K) and the field scans at 300 K and 40 K at 51.2 MHz and 30.2 MHz, we find a good agreement of the values which is a strong indication of having second-order quadrupole effects. The corresponding mean values are $\bar{\nu}_Q(40\,\text{K}, 300\,\text{K}) = 3.4(3)$ MHz, and $\bar{\nu}_Q(4\,\text{K}) = 4.7(7)$ MHz.

We note here that the Lorentz-fit approach (equation (6.1)) does not exactly match the theoretical expectations. Taking peak B as 6 broadened satellites, a reduced intensity towards the center position would be expected, which is not the case in the Lorentz-fit function (see figure 6.2 on the upper left panel). Nevertheless equation (6.1) still gives an accurate result for calculating the FWHM of the peaks.

An additional indication for second-order quadrupole effects ($1/B_0$ dependence) is the asymmetry of the field-scan data in comparison with the symmetrical Lorentz-fit that is

frequency/field	T [K]	Δ_{A_B} [G]	Δ_{A_ν} [kHz]	Δ_{B_B} [G]	Δ_{B_ν} [kHz]	ν_Q [MHz]
8.5 T	300	419(80)	260(50)	4869(900)	2933(600)	3.1(6)
51.2 MHZ	300	599(50)	361(30)	8222(800)	4952(500)	3.6(3)
51.2 MHZ	40	660(50)	397(30)	6720(600)	4048(400)	3.8(3)
51.2 MHZ	4	1123(350)	676(200)	5883(900)	3544(600)	4.9(9)
30.2 MHZ	300	919(90)	554(60)	7573(700)	4562(500)	3.5(4)
30.2 MHZ	40	750(70)	452(40)	7196(700)	4335(500)	3.1(3)
30.2 MHZ	4	1446(150)	871(80)	6924(700)	4171(500)	4.4(5)

Table 6.2: The Δ's and ν_Q summary from ^{139}La frequency and field scans.

clearly visible in the example shown in figure 6.9. The same asymmetry is observed in all the field scans, but not in the frequency scan at room temperature.
Even if second order quadrupole effects are present, the possibility of magnetic effects can not be excluded. With magnetic effects we would expect a constant or higher FWHM for higher fields.

Up to now, the focus of our discussion was on the field dependence of the data. We now want to briefly discuss the temperature dependence. We see a clear loss of intensity below 80 K, with an intensity minima at 20 K (see figure 6.7). The ratio between the top of peak A (A_C) and the crossover points to peak B (average of AB_L and AB_R) also indicates a loss of intensity of the central peak A below 20 K (see figures 6.3, 6.4, and 6.8).

Possible explanations for this increase in the signal width and the loss of intensity at low temperatures are:

- The possible oxygen diffusion in the lattice due to the oxygen deficiency in LaBaNiO$_{4-\delta}$ slows down or even freezes out at lower temperatures, producing a broadening of the ^{139}La signal due to differing EFG's at different ^{139}La lattice sites.
  At higher temperatures this oxygen diffusion is too fast to be seen on NMR times scale (faster than $1/\Delta_\nu$).

- A magnetic Ni-spin ordering occurs at low temperatures, that leads to a magnetic broadening of the ^{139}La spectrum.

Both scenarios can create, in extreme cases, even a possible wipe-out phenomenon analogous to Ref. [13].

To conclude this discussion, we state that it is difficult to interpret the NMR measurements on LaBaNiO$_{4-\delta}$ due to its oxygen deficiency. We have observed a second order quadrupolar field dependence ($1/B_0$) with a ν_Q around 4 MHz, and a decrease of the spin signal with decreasing temperature, specially of peak A. This might be attributed either to
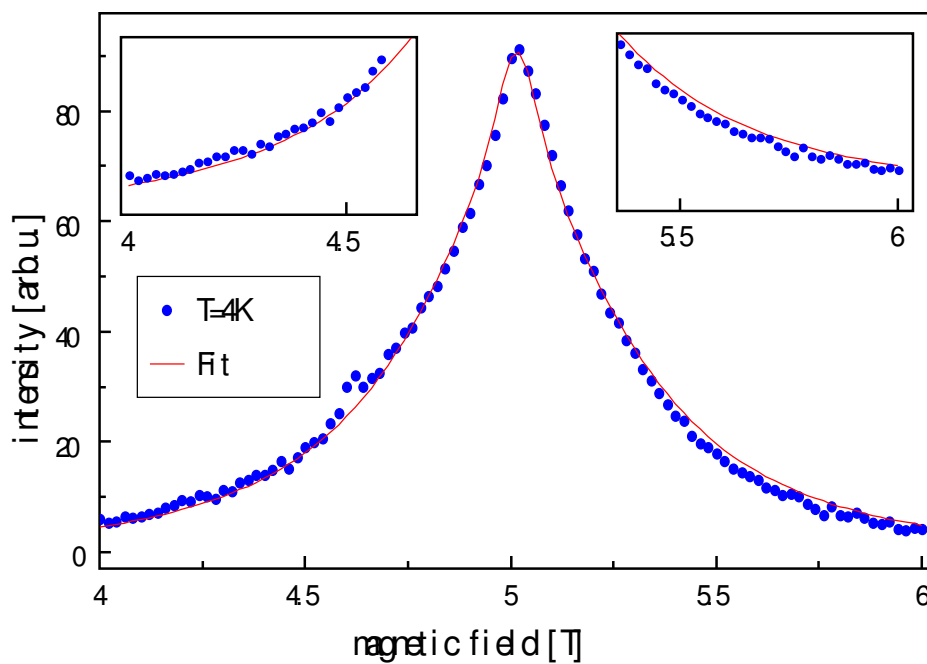
Figure 6.9: Representative second-order quadrupole asymmetry between the data points and the symmetrical Lorenz-fit. Data of the field scan at 4 K, 31.2 MHz.

a freezing out of the oxygen diffusion or/and to a magnetic Ni-spin ordering.

Nevertheless, NMR can still be a very powerful tool to examine $LaBaNiO_{4-\delta}$ provided that we can improve the sample quality by minimizing the oxygen deficiency. To ensure full oxygenation, high oxygen-pressure annealing-techniques will have to be applied.

Chapter 7

Summary and Outlook

For this diploma thesis a new NMR probe head was constructed to be used in the PPMS (Quantum Design), which offers the possibility to vary the magnetic field between $0\,\mathrm{T}$ and $9\,\mathrm{T}$, and to cool a sample down below $2\,\mathrm{K}$. For the design of the NMR probe head the construction materials had to be chosen according to spacial, thermal, magnetic, and electric criteria. The functionality of the probe head was tested in the PPMS, giving us information about the behavior of the system upon cooling, the magnetic stability and homogeneity. The probe head showed good performance, easy handling and mechanical stability at high magnetic fields and at low temperatures.
Moreover, the NMR probe head can be used for different NMR and low temperature NQR experiments.
The magnetic homogeneity of the PPMS corresponds to the specifications given by the manufacturer. A slight drift of the magnetic field was noticed using the oscillating-approach mode to change fields, but this was not of concern for the present investigation.

A $70\,\mathrm{MHz}$ spectrometer was built consisting out of industrial RF devices. The spectrometer unit was successfully tested, but showed fairly weak amplification and overload problems after a pulse. The amplification could be increased by using an additional amplifier. The overload problem was solved by attenuation in the transmitter path.
The spectrometer has no capability of handling phases as the spectrometers from the Lupotto series. However, phase modulations can be done by using a fast phase switchable frequency generator.

Finally, an NMR investigation on the polycrystalline compound $LaBaNiO_{4-\delta}$ has been carried out. Frequency, magnetic field, and temperature scans on the ^{139}La nuclei and magnetic field scans on the ^{137}Ba and ^{135}Ba nuclei were performed. Possibly due to a certain oxygen deficiency in the sample, the spectral lines are broadened, which makes an interpretation difficult.
The measurements on ^{139}La showed the presence of second order quadrupole effects.
A broadening and decrease of intensity of the central peak at low temperatures is observed. Slowing down or even freezing out of oxygen diffusion (due to the oxygen deficiency) and/or

a magnetic Ni-spin ordering may explain this broadening at low temperatures.

The spin signals of the ^{137}Ba and the ^{135}Ba nuclei are visible but not conclusive within the limited time range of this diploma thesis.

A reduction of the oxygen deficiency in LaBaNiO$_{4-\delta}$ by high oxygen-pressure annealing-techniques in order to obtain more conclusive NMR data is highly desirable.

Appendix A

Code of "fldscan1" Function Script

In this appendix section the code of our fieldscan measurements is presented. The explanations for this code are given in section 3.4.

```
function dummy = fldscan1(name,f_begin,f_step,f_end,query)

%function lecory =  fldscan1(name,f_begin,f_step,f_end,query)

%name  file name for saving of data
%f_begin in Oersted
%f_step in Oersted
%f_end in Oersted
%query (=1, for param. input by query, =0 for param. by direct editing, see below)
%
%output of LeCroy data in matrix lecroy and
%output of integrated intensity in matrix echointens
%4 loop trigger E cycle (phase correction)


if query ==1,

% input of parameters by query:
%
tau =input('tau in ms ? ');
RR = input('repetition time in ms ? ');
sweeps=input('how many sweeps ? ');
bc_window = input('how large is bc_window (in points) ? ');
i_left = input('integration interval, left edge (in points) ? ');
i_right = input('integration interval, right edge (in points) ? ');
%
else,
```

```
%
%OR input of parameters by direct editing right here:
%
tau = 0.02;
RR = 50;
sweeps = 1000;
bc_window = 200;
i_left = 270;
i_right = 775;

end;

fig_h=figure('Position',[5 220 320 320]);plot(1);

mes_dat =[];echointens=[]; ppms_temperature=[]; cernox_Resist=[];
initgpib;
%pause(10);
for f = f_begin:f_step:f_end
tic;

%*********************set field*********************************************
flag=0;
f_str=int2str(f);
sendgpib(15,['FIELD ' f_str ' 100 2;']);
pause(20);
while flag ==0,
status=readgpib(15,['GETDAT? 1;']);
Ix = find(status==',');Ix_max=find(status==';');
HEX=dec2hex(str2num(status(Ix(2)+1:Ix_max-1)));

if str2num(HEX(3)) == 1,
flag=1;pause(5);
end;
%disp('sch....');
end;
%disp('OK');

%***********************read field value and temperature*******************

ppms_data=readgpib(15,['GETDAT? 22;']);
Ix = find(ppms_data==',');Ix_max=find(ppms_data==';');
ppms_temp = str2num(ppms_data(Ix(2)+1:Ix(3)-1));
field_value =  str2num(ppms_data(Ix(3)+1:Ix(4)-1));
```

```
cernox_R =  str2num(ppms_data(Ix(4)+1:Ix_max-1));



t2seq14('scratch',sweeps,tau,RR);
load scratch;
signal =pp_pcdif(lc9410_messung);

echoint = echoeval(signal,bc_window,i_left,i_right);
echointens = [echointens; field_value echoint];

ppms_temperature = [ppms_temperature; ppms_temp];
cernox_Resist = [cernox_Resist; cernox_R];
signal(1,2)=field_value;

        if f == f_begin;
          mes_dat=signal;
        else
          mes_dat = append(mes_dat,signal);
        end




eval(['save ' name ' echointens ppms_temperature cernox_Resist mes_dat']);

figure(fig_h);plot(echointens(:,1),abs(echointens(:,2)),'o');

elTim =toc; disp(['elapsed time in min. = ' num2str(elTim/60)]);

end;
```

Appendix B

Calibration of the *CERNOX* Temperature Sensor

For the 4-terminal resistivity measurement, the sample is mounted on the resistivity sample puck and connected to the ports. This sample puck is conceived to measure 3 samples at the same time. With a special tool the puck is inserted into the PPMS. Through the user bridge the different channels are read out. The temperature dependant resistivity is now easily measured by creating an automated sequence.[B.1]

[B.1]The data is deposited in the PPMS computer folder: `C:\QdPpms\Data\alex\cernoxCal`
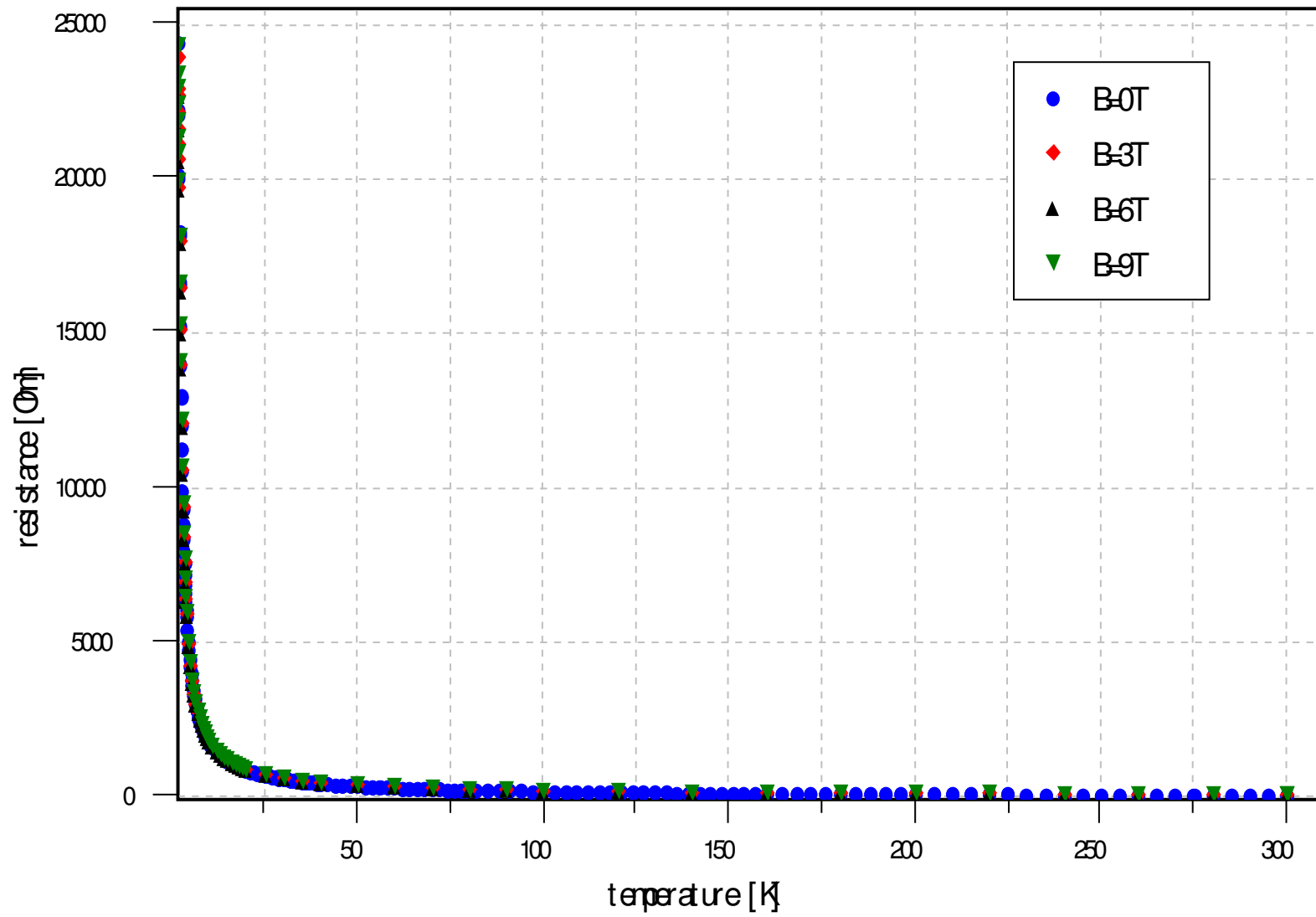
Figure B.1: Calibration measurements for the CERNOX temperature sensor.

Appendix C

70 MHz Spectrometer: Connectors and RF Elements

The connectors pin lineup for the spectrometer and the power supply, and the list of RF elements are presented in this appendix.

C.1 Connectors lineup

The given switch numbers are the ones described in section 4.2.1 and the schematic seen in figure 4.6 in page 38. The spectrometer has 2 ports, the spectrometer TTL signal and the power lines. The power supply is directly connected to this two ports and receives the TTL signal from the Pulse Controller PC.
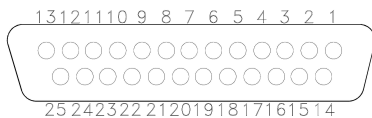
C.1.1   70 MHz spectrometer

Figure C.1
Steer Bridge Port
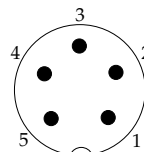
Figure C.2
Power Connector

PIN	switch
2	9
5	12
8	3
11	21
14 − 25	GND

PIN	voltage
1	−5 V
2	GND
3	+5 V
4	GND
5	+15 V

C.1.2   Power supply
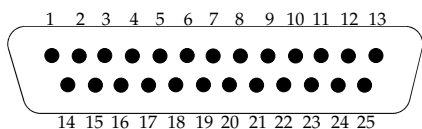
Figure C.3
Steer Bridge Port

Figure C.4
PC Steer Port

Figure C.5
Power Connector

PIN	Switch
2	9
5	12
8	3
11	21
14 − 25	GND

PIN	steer TTL
1	PC steer
6	GND
7	GND
8	GND
9	GND

PIN	voltage
1	−5 V
2	GND
3	+5 V
4	GND
5	+15 V

C.2 List of RF elements

Dev.	device type	model number	supplier	+5V(mA)	-5V(mA)	+15V(mA)
1	Frequency multiplier	LNOM-10-7-10-17	Wenzel Ass.			410
2	Bandpass filter	SBP-70	Mini-Circuits			
3	TTL switch	ZYSWA-2-50DR	Mini-Circuits	20	20	
4	Attenuator	VAT-	Mini-Circuits			
5	Frequency mixer	ZEM-2B	Mini-Circuits			
6	Lowpass filter	SLP-300	Mini-Circuits			
7	Attenuator	VAT-	Mini-Circuits			
8	Amplifier	ZFL-500	Mini-Circuits			80
9	TTL switch	ZYSWA-2-50DR	Mini-Circuits	20	20	
	$50\,\Omega$ termination	ANNE	Mini-Circuits			
10	Variable attenuator	50TA-006 SMA (F) JFW	Emitec			
11	Lowpass filter	BLP-	Mini-Circuits			
12	TTL switch	ZYSWA-2-50DR	Mini-Circuits	20	20	
14	I & Q Attenuator	ZFMIQ-70D	Mini-Circuits			
15	Bandpass filter	SBP-70	Mini-Circuits			
16&18	Frequency multiplier	LNOM-10-7-10-17	Wenzel Ass.			410
	Amplifier	ZFL-500LN	Mini-Circuits			60
19	Bandpass filter	SBP-70	Mini-Circuits			
20	Frequency mixer	ZEM-2B	Mini-Circuits			
21	High isolation TTL switch	ZYSWA-2-50DR	Mini-Circuits	60	60	
22	Variable attenuator	50TA-007 SMA (F) JFW	Emitec			
23	Attenuator	VAT-	Mini-Circuits			
24	Attenuator	VAT-	Mini-Circuits			
25	Attenuator	VAT-	Mini-Circuits			
	Total power consumption for RF elements			**120**	**120**	**960**

Bibliography

[1] A. Abragam, *The Principles of Nuclear Magnetism*, Oxford University Press, UK (1961)

[2] C. P. Slichter, *Principles of Magnetic Resonance*, Springer-Verlag, Germany (1990)

[3] G. C. Carter/L. H. Bennet/D. J. Kahan, *Metallic Schifts in NMR*, Part I, Pergamon Press, USA

[4] Quantum Design, *Physical Property Measurement Manual, Hardware Manual*, USA (2000)

[5] Quantum Design, *Physical Property Measurement Manual, Software Manual*, USA (2000)

[6] Quantum Design, `www.qdusa.com`, USA

[7] H. Meinke/F.W. Grundlach, *Taschenbuch der Hochfrequenztechnik*, Springer-Verlag, Germany (1956)

[8] M. Weller, `http://cryo-nmr.ethz.ch/~mweller/Spectrometer/`, Solid State Physics Laboratory, ETHZ, Switzerland

[9] A. Schilling, *Synthesis and characterization of LaBaNiO$_{4-\delta}$* , MaNEP Year 5 Report, Project 4, University of Zürich (2006)

[10] G. Demazeau et al., Mat. Res. Bull. **17**, 37 (1982)

[11] J. A. Alonso et al., Solid State Commun. **76**, 1327 (1990)

[12] R. J. Cava et al., Phys.Rev. **B 42**, 1229 (1991)

[13] I. M. Abu-Shiekah et al., Phys. Rev. Lett. **83**, 3309 (1999)

[14] I. M. Abu-Shiekah et al., Phys. Rev. Lett. **87**, 237201 (2001)

[15] A. Mehta/P. J. Heaney, Phys. Ref. **B 49**, 563 (1994)

[16] M.Bankay, *Kernresonanz an Y-Ba-Cu-O-Supraleitern*, Dissertation, Universität Zürich (1995)